

AD-A057 402

STANFORD UNIV CALIF DEPT OF CIVIL ENGINEERING
THE GROWTH OF OCEAN WAVES UNDER THE ACTION OF THE WIND.(U)
JUN 78 C HSU, F CHEN, E HSU, R L STREET

F/G 8/3

UNCLASSIFIED

TR-228

ARO-13145.2-GS

DAAG29-76-G-0125

NL

1 OF 1
AD
A057402



AD A057402

AD No. _____
DDC FILE COPY

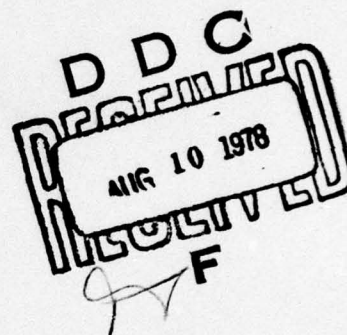
Technical Report No. 228


LEVEL II

FINAL REPORT ON THE GROWTH OF OCEAN WAVES UNDER THE ACTION OF THE WIND

by

Chin-Tsau Hsu
Fang-Jenq Chen
En-Yun Hsu
Robert L. Street



This research was supported by
U.S. Army Research Office
Grant No. DAAG 29-76-G-0125

June 1978

Approved for Public Release;
Distribution Unlimited



Department of CIVIL ENGINEERING
STANFORD UNIVERSITY

78 08 07 180

THE FINDINGS OF THIS REPORT ARE NOT TO BE CONSTRUED AS
OFFICIAL DEPARTMENT OF THE ARMY OR DEPARTMENT OF THE
NAVY POSITION, UNLESS SO DESIGNATED BY OTHER
AUTHORIZED DOCUMENTS.

REPORT DOCUMENTATION PAGE		READ INSTRUCTIONS BEFORE COMPLETING FORM
1. REPORT NUMBER (19) 13145.2-GS	2. REPORT ACCESSION NO. (18) ARD	3. RECIPIENT'S CATALOG NUMBER
4. TITLE (and Subtitle) (6) The Growth of Ocean Waves Under the Action of the Wind,		5. TYPE OF REPORT & PERIOD COVERED (9) Final Report 1 Jan 76 - 30 Jun 78
7. AUTHOR(s) (10) Chin-Tsau/Hsu, Fang-Jeng/Chen, En-Yun/Hsu Robert L./Street		8. CONTRACT OR GRANT NUMBER(s) (15) DAAG29-76-G-0125
9. PERFORMING ORGANIZATION NAME AND ADDRESS Stanford University Stanford, California		10. PROGRAM ELEMENT, PROJECT, TASK AREA & WORK UNIT NUMBERS
11. CONTROLLING OFFICE NAME AND ADDRESS U. S. Army Research Office P. O. Box 12211 Research Triangle Park, NC 27709		12. REPORT DATE (11) June 78
14. MONITORING AGENCY NAME & ADDRESS (if different from Controlling Office) (12) 55P		13. NUMBER OF PAGES 56
16. DISTRIBUTION STATEMENT (of this Report) Approved for public release; distribution unlimited. (14) TR-228		15. SECURITY CLASS. (of this report) unclassified
17. DISTRIBUTION STATEMENT (of the abstract entered in Block 20, if different from Report)		15a. DECLASSIFICATION/DOWNGRADING SCHEDULE
18. SUPPLEMENTARY NOTES The findings in this report are not to be construed as an official Department of the Army position, unless so designated by other authorized documents.		
19. KEY WORDS (Continue on reverse side if necessary and identify by block number)		
20. ABSTRACT (Continue on reverse side if necessary and identify by block number) This study provides some insight to the differences between the wave-induced flow quantities measured in a fixed and wave-following transformed coordinate system. The wave-induced quantities have different flow characteristics depending on the relative magnitude of the mean free stream speed with respect to the wave celerity. In order to detect the instantaneous critical layer mechanism associated with the modified Miles' theory, a wind speed just above the wave celerity should be used. 400 117		

FINAL REPORT
ON
THE GROWTH OF OCEAN WAVES UNDER
THE ACTION OF THE WIND

by

Chin-Tsau Hsu
Fang-Jenq Chen
En-Yun Hsu
Robert L. Street

This research was supported by
U.S. Army Research Office
Grant No. DAAG 29-76-G-0125

June 1978

Approved for Public Release;
Distribution Unlimited.

78 08 07 180

ABSTRACT

This study provides some insight to the differences between the wave-induced flow quantities measured in a fixed and wave-following transformed coordinate system. The wave-induced quantities have different flow characteristics depending on the relative magnitude of the mean free stream speed with respect to the wave celerity. In order to detect the instantaneous critical layer mechanism associated with the modified Miles' theory, a wind speed just above the wave celerity should be used.

ACCESSION for	
NTIS	White Section <input checked="" type="checkbox"/>
DDC	Buff Section <input type="checkbox"/>
UNANNOUNCED	<input type="checkbox"/>
JUSTIFICATION	
BY	
DISTRIBUTION/AVAILABILITY CODES	
Dist.	SP. CIAL
A	

TABLE OF CONTENTS

1.	INTRODUCTION	1
2.	THEORETICAL ASPECTS	6
2.1	Momentum and Energy Transfer from Wind to Waves -- a Modified Miles' Theory	6
2.2	Transformed Wave-Following Coordinate System . . .	12
3.	EXPERIMENTAL APPARATUS AND INSTRUMENTATION	15
3.1	The Air-Water Channel	15
3.2	Wave-Follower System	16
3.3	Instrumentation and Calibration	17
4.	DATA ACQUISITION AND REDUCTION	20
5.	EXPERIMENTAL RESULTS	22
5.1	Mean Air Flowfield	22
5.2	Wave-Induced Flowfield	23
5.2a	No Critical Layer Case ($U_{\infty}/c = 0.93 < 1$)	24
5.2b	Critical Layer Flow (Low Critical Layer, $U_{\infty}/c = 1.87 < 1$)	25
5.3	Probability Distribution $\alpha(y)$	27
6.	CONCLUDING REMARKS.	29
	REFERENCES	30
	TABLES	33
	LIST OF FIGURES	35

1. INTRODUCTION

The momentum and energy transfer from the wind to water waves on the surface of the ocean is a major geophysical phenomena. In the past two decades many efforts have been made to gain a complete understanding of the processes responsible for the generation and the growth of the water waves. Neumann's wave spectrum concept was an important advance, but the first significant contributions to the dynamical wave theory were contained in Phillips (1957) and Miles (1957).

Phillips' (1957) resonance mechanism describes the response of the water surface to the direct action of air turbulent pressure fluctuations and is responsible for the initiation of the water waves. The wave growth rate associated with this mechanism is linear.

Miles' (1957) inviscid, quasi-laminar, instability mechanism includes the feedback of air perturbations due to water waves to the waves themselves. The weaknesses of this mechanism are the resulting infinite vorticity at the "critical height" where the mean wind velocity is equal to the phase velocity of the waves and the requirement of a free-slip boundary condition at the interface. These difficulties were overcome later by Miles (1959) and Benjamin (1959) by retaining viscous effects to form a "critical layer" near the critical height and a viscous layer at the interface. However, there are no obvious differences between the results from the inviscid model and from the viscous model. Hence, for energy transfer from the wind to the waves, the inviscid model appears to remain valid. The physical key to Miles' theory is that the component of pressure perturbations in phase with the wave slope, this component being the driving force for the energy transfer, is present due to the existence of the critical layer. Therefore, one

concludes that the critical layer has an important role in the momentum and energy transfer from the wind to the waves. The growth rate of water waves according to this model is exponential.

The equations involved in both Phillips' and Miles' processes are linear, that is, the components of pressure fluctuations and of water waves with the same frequency and wave-number are linearly related. In their models, nonlinear effects produced by the interactions among the components of turbulence and wave perturbations at different frequencies and wave-numbers are ignored. Experimental results both in the field [Snyder and Cox (1966), Barnett and Wilkerson (1967), and Dobson (1971)] and in the laboratory [Bole and Hsu (1969) and Stewart (1970)] showed that the observed wave growth rates are one order of magnitude greater than those predicted by Miles' theory. There are other experimental measurements which lead either directly or indirectly to similar conclusions. This inconsistency between predictions and observations suggested a re-examination of the role of turbulence which was originally neglected in Miles' formulation.

To evaluate the turbulent effect, one approach which has been used most frequently is to construct a numerical model for the wave perturbation field by retaining the wave-induced turbulent Reynolds stresses in the linearized wave perturbation equations. Unfortunately, this type of approach has been greatly hindered by the associated closure problem. Several closure models have been proposed (Long, 1971; Davis, 1970, 1972; Townsend, 1972; Saeger and Reynolds, 1971; Norris and Reynolds, 1975; and Gent and Taylor, 1976). None of these models led to a satisfactory prediction of the wave growth rate. All the models were based on ad hoc or phenomenological assumptions

necessitated by the lack of accurate experimental data on the induced turbulent Reynolds stresses. According to Davis (1970, p. 730), "the problem of wave generation cannot be understood until the wave's influence on the turbulent stresses is known." A direct measurement of the wave perturbation field including the induced turbulent Reynolds stresses seems to be an expeditious way to reveal the wave perturbed flow field and hence to achieve successful closure modeling.

A measurement of the induced turbulent Reynolds stresses was first attempted by Kendall (1970) and subsequently at Stanford by Yu, et al. (1973) and Chao, et al. (1976). However, the first conclusive and complete set of data on the induced turbulent Reynolds stresses was presented by Hsu, et al. (1977). One interesting feature shown in Hsu, et al. is that an eddy viscosity type of closure model seems appropriate for the induced turbulent Reynolds stresses.

In addition to searching for a closure model, a complementary approach is to evaluate directly the turbulent effect on the Miles' mechanism. When turbulence exists, the role of viscosity in smoothing the concentrated vorticity distribution in the critical layer is taken over by the more diffusive turbulent mixing. The physical significance of the turbulent effect on the critical layer structure was first acknowledged by Lighthill (1962) and then followed up by Stewart (1967, 1974). According to Lighthill, the turbulence effect was supposed to broaden the critical layer and to render Miles' mechanism more efficient. But, the extent of the enhancement of the energy transfer from the wind to the waves due to the turbulence was not estimated by Lighthill. The Hasselmann's (1968) theory also suggested that the turbulence will cause the critical layer to extend over a wide range of the wind velocity profile.

The turbulent effect on the wave generation processes is twofold: (a) to transfer directly the energy from wind to waves through the induced turbulent Reynolds stresses, and (b) to enhance the Miles' mechanism by changing the characteristics of the critical layer. Because the energy contained in the turbulence is relatively small compared with the amount of energy required for the wave growth, Stewart (1967) inferred that transfer (a) should be insignificant. He also interpreted transfer (b) in terms of the so-called "catalytic effect". The concept of the catalytic effect was further extended by Stewart (1974) through examining and comparing the transfer by Miles' mechanism while using either the mean velocity profile or the instantaneous velocity profiles, as measured by Kim, et al. (1971). The visual studies of Kim, et al. suggested that approximately 90 percent of the turbulent Reynolds stress is produced during a wave-like "bursting" process. Their measured turbulent Reynolds stress was also consistent with their prediction based on the measured instantaneous velocity profiles. Hence, it seems likely that the wave-associated Reynolds stress can be regarded as the statistical average of those stresses produced by the critical layer mechanism according to the instantaneous velocity profiles. These concepts and the philosophy of Davis (1974, p. 673), that "all averaging is delayed until the dynamical equations have been solved ...", has enabled us to consolidate the turbulent catalytic effect into mathematical expressions. The result is then regarded as a modified Miles' theory.

The experimental aspect of this research program contains two facets. One is the study of the structure of the wave-induced flowfield, especially for the wave-induced turbulent Reynolds stresses which form the kernel of the closure problem. The other is the study of the turbulent effect on

the structure of critical layer as it appears in our modified Miles' theory; the details of which are given in Section 2. For the first facet, we extended the measurements of Hsu, et al. (1977), which were performed at a mean free stream velocity of 2.4 m/sec and in a wave-following, transformed coordinate system, to mean free stream velocities of 1.4 and 2.9 m/sec and to the inclusion of a fixed frame measurement to examine the difference between fixed frame and transformed frame measurements under identical experimental conditions. For the second facet, we measured the instantaneous velocity gradient by using two X-array hot-film probes separated vertically by 1.2 cm. The statistical properties of the instantaneous velocity gradient are the key to the evaluation of the modified Miles' theory as shown in Section 2. The facility used for the experiment is described in Section 3; the data acquisition and reduction are then given in Section 4. In Section 5 we describe the experimental results, followed by a concluding remark (Section 6).

2. THEORETICAL ASPECTS

2.1 Momentum and Energy Transfer from Wind to Waves -- a Modified Miles' Theory

Consider a turbulent wind flowing over a sinusoidal water wave which propagates in the x-direction and is given by $\tilde{\eta} = a \cdot \cos(kx - \omega t)$, where a is the wave amplitude, k is the wave-number and ω is the circular wave-frequency. The vorticity equation in the lateral (z-direction) can be obtained by eliminating the pressure terms in the momentum equations in the x- and the (vertical) y-directions. The resultant equation is

$$\begin{aligned} \frac{\partial}{\partial t} \left(\frac{\partial u}{\partial y} - \frac{\partial v}{\partial x} \right) + \frac{\partial}{\partial x} \left[\frac{\partial}{\partial y} (uu) - \frac{\partial}{\partial x} (uv) \right] + \frac{\partial}{\partial y} \left[\frac{\partial}{\partial y} (uv) - \frac{\partial}{\partial x} (vv) \right] \\ + \frac{\partial}{\partial z} \left[\frac{\partial}{\partial y} (uw) - \frac{\partial}{\partial x} (vw) \right] = \nu \nabla^2 \left(\frac{\partial u}{\partial y} - \frac{\partial v}{\partial x} \right) \end{aligned} \quad (2.1)$$

where ν is the kinematic viscosity, $\nabla^2 = (\partial^2/\partial x^2) + (\partial^2/\partial y^2) + (\partial^2/\partial z^2)$ and u , v , and w are the velocity components in the x , y , and z directions respectively. In (2.1) we have assumed that the air is incompressible so that the continuity equation is

$$\frac{\partial u}{\partial x} + \frac{\partial v}{\partial y} + \frac{\partial w}{\partial z} = 0 \quad (2.2)$$

We assume that the mean flow is parallel, i.e., $\bar{u} = \bar{u}(y)$, $\bar{v} = 0$, and $\bar{w} = 0$, and that the wave-induced flow is two dimensional in (x, y) . Hence, we have

$$\begin{aligned} u &= \bar{u}(y) + \tilde{u}(x, y, t) + u'(x, y, z, t) \\ v &= \tilde{v}(x, y, t) + v'(x, y, z, t) \\ w &= w'(x, y, z, t) \end{aligned} \quad (2.3a, b, c)$$

Here " \sim " denotes a wave-induced component and "'" denotes turbulent fluctuations, while, in order to separate the mean and the wave-induced quantities from the background turbulence, we define a time average as

$$\bar{g} = \lim_{T \rightarrow \infty} \frac{1}{T} \int_{-T/2}^{T/2} g(\underline{x}, t) dt \quad (2.4)$$

and a phase average as

$$\langle g \rangle = \lim_{N \rightarrow \infty} \frac{1}{2N+1} \sum_{n=-N}^N g(\underline{x}, t+n\tau) \quad (2.5)$$

where g is a flow quantity of interest, \underline{x} is the position vector at which the averages are performed and τ is the period of wave oscillation. The wave-induced flow then can be found from

$$\tilde{g} = \langle g \rangle - \bar{g} \quad (2.6)$$

The vorticity in the z -direction is given by

$$\Omega = \frac{\partial u}{\partial y} - \frac{\partial v}{\partial x} = \bar{\Omega}(y) + \tilde{\Omega}(x, y, t) + \Omega'(x, y, z, t) \quad (2.7)$$

Hence,

$$\bar{\Omega} = \frac{\partial \bar{u}}{\partial y}, \quad \tilde{\Omega} = \frac{\partial \tilde{u}}{\partial y} - \frac{\partial \tilde{v}}{\partial x}, \quad \Omega' = \frac{\partial u'}{\partial y} - \frac{\partial v'}{\partial x} \quad (2.8a,b,c)$$

by substituting (2.3a,b,c) into (2.7).

When (2.3a,b,c) and (2.7) are substituted into (2.1), the resultant equation is first time and then phase averaged and the time-averaged result is subtracted from the phase-averaged result, we find

$$\begin{aligned} \frac{\partial \tilde{\Omega}}{\partial t} + \bar{u} \frac{\partial \tilde{\Omega}}{\partial x} + \tilde{w} \frac{\partial^2 \bar{u}}{\partial y^2} &= \left(\frac{\partial^2}{\partial x^2} - \frac{\partial^2}{\partial y^2} \right) (\tilde{r}_{12} + \tilde{s}_{12}) \\ - \frac{\partial^2}{\partial x \partial y} (\tilde{r}_{11} - \tilde{r}_{22} + \tilde{s}_{11} - \tilde{s}_{22}) &+ \nu \left(\frac{\partial^2}{\partial x^2} + \frac{\partial^2}{\partial y^2} \right) \tilde{\Omega} \end{aligned} \quad (2.9)$$

$$\tilde{r}_{ij} = \langle u'_i u'_j \rangle - \overline{u'_i u'_j} \quad (2.10)$$

and

$$\tilde{s}_{ij} = \tilde{u}_i \tilde{u}_j - \overline{\tilde{u}_i \tilde{u}_j} \quad (2.11)$$

It has been shown by Davis (1969) and Hsu, et al. (1978) that \tilde{s}_{ij} is related to the nonlinear effect of the wave-induced motion and irrelevant to the momentum and energy transfer from wind to waves, although the wave-induced flow structure may be different for a large amplitude wave.

Under the small amplitude assumption on the water wave, \tilde{s}_{ij} can be safely neglected, since it is only of order $(ka)^2$. On the other hand, the terms with \tilde{r}_{ij} in (2.9) are of order (ka) and are assumed to be significant in changing the wave-induced flow structure relevant to the momentum and energy transfer from wind to waves. However, the inclusion of \tilde{r}_{ij} in (2.9) raises the well known "closure" problem because the \tilde{r}_{ij} are the additional unknowns which make the problem unsolvable unless some closure relations are assumed. The viscous terms in (2.9) are usually negligible when \tilde{r}_{ij} is included in (2.9), except near the interface where the turbulence is damped out by viscosity.

It must be pointed out that the application of the averaging procedures here has simplified the problem by artificially restricting the critical layer in a mean sense to a region near the definite position where $\bar{u} - c = 0$. Furthermore, it also forced us to rest the solution of (2.9) entirely on the closure relations associated with the wave-induced turbulent Reynolds stresses \tilde{r}_{ij} . A successful closure model should not only lead to a description of the effect of turbulence in changing the structure of critical layer as related to the wave-induced motion, but also to a prediction of precisely the amount of momentum and energy transfer from wind to waves. Unfortunately, to date, there exists no such applicable model.

It is important to note that in a real flow the effects of non-linearity and of turbulence will change the location of the critical layer from time to time according to $\bar{u} + \tilde{u} + u' - c = 0$. Thus, the slope and the curvature at the critical height at any time are strongly influenced by these effects. Stewart (1974) suggested that the mean velocity profile was not the appropriate thing and that consideration of the instantaneous velocity profile would be helpful in describing the energy transfer from wind to waves. In order to keep the spirit of his "catalyst effect," after substituting (2.3a,b,c) into (2.1) and subtracting the time average of the resultant equation from the resultant equation, the difference can be written as

$$(u - c) \frac{\partial \tilde{\Omega}}{\partial x} = T' + \tilde{f}_n - \tilde{v} \frac{\partial^2 \tilde{u}}{\partial y^2} + \tilde{f} + \tilde{f}_v \quad (2.12)$$

when $\frac{\partial \tilde{\Omega}}{\partial t} = -c \frac{\partial \tilde{\Omega}}{\partial x}$ is applied. In (2.12), T' is the term containing no organized component, i.e., $\langle T' \rangle = 0$; \tilde{f}_n is the nonlinear term containing $\tilde{u} \frac{\partial \tilde{u}}{\partial y}$ etc.; and \tilde{f} and \tilde{f}_v are expressed as

$$\tilde{f} = \left(\frac{\partial^2}{\partial x^2} - \frac{\partial^2}{\partial y^2} \right) \tilde{r}_{12} - \frac{\partial^2}{\partial x \partial y} (\tilde{r}_{11} - \tilde{r}_{22}) \quad (2.13)$$

and

$$\tilde{f}_v = v \left(\frac{\partial^2}{\partial x^2} + \frac{\partial^2}{\partial y^2} \right) \tilde{\Omega} \quad (2.14)$$

respectively.

Since, we are interested in the role of the instantaneous velocity profile in the framework of traditional Miles' theory, T' and \tilde{f}_n in (2.12) can be ignored. The solution for $\tilde{\Omega}$ in the limit of very high Reynolds number can be found from (2.12) by letting \tilde{f}_v be zero while admitting a singularity at y_c where $u - c = 0$ as generally imposed in the inviscid theory. To the first order approximation in ka , $\tilde{\Omega}$, \tilde{v} , and \tilde{f} are sinusoidal functions of x . By dividing (2.12) by $(u - c)$ and taking the phase average, we have

$$\begin{aligned} k\tilde{\Omega}(x, y, t) &= \frac{\partial \tilde{\Omega}}{\partial x} \left(x - \frac{\pi}{2k}, y, t \right) \\ &= \left[\frac{\partial^2 u}{\partial y^2} / (u - c) \right] \cdot \tilde{v} \left(x - \frac{\pi}{2k}, y, t \right) \\ &\quad + \left[1 / (u - c) \right] \cdot \tilde{f} \left(x - \frac{\pi}{2k}, y, t \right) \end{aligned} \quad (2.15)$$

Note that in reaching (2.15), the dynamical equation for the vorticity is solved before the phase average is taken, as emphasized by Davis (1974).

Hsu, et al. (1977) showed that the momentum and energy transfer from wind to waves is mainly produced by the wave-induced pressure which is supported by the wave form to give momentum flux and acts against the

vertical oscillation to do work. The momentum and energy transfer by the induced pressure can also be interpreted in terms of the wave-associated Reynolds stress. According to Lighthill (1962), the wave-associated Reynolds stress $\tau_w(y)$ is produced from the transport of the wave induced vorticity $\tilde{\Omega}(x,y,t)$ by the wave-induced vertical velocity $\tilde{v}(x,y,t)$, i.e.,

$$\tau_w(y) = -\rho \overline{\tilde{u}\tilde{v}}(y) = \rho \int_y^\infty \overline{\tilde{\Omega}\tilde{v}}(\xi) d\xi \quad (2.16)$$

Because only the component of $\tilde{\Omega}(x,y,t)$ in phase with $\tilde{v}(x,y,t)$ can correlate with \tilde{v} to produce the wave-associated Reynolds stress, the first term on the right hand side of Eq. (2.15) contributes only in the critical layer. However, the second term can contribute either when $u = 0$ or $u \neq 0$ depending on the phase of \tilde{f} relative to \tilde{v} . Substituting Eq. (2.15) into Eq. (2.16) and applying the residual theorem of complex analysis, we find

$$\begin{aligned} \tau_w(y) = & \rho \int_y^\infty \overline{\tilde{v}^2} \left(\frac{\partial^2 u}{\partial y^2} \right)_{\xi=y_c} \alpha(\xi) d\xi + \rho \int_y^\infty \tilde{f}\tilde{v} \left(\frac{1}{\partial u / \partial y} \right)_{\xi=y_c} \alpha(\xi) d\xi \\ & + \rho \int_y^\infty \overline{\tilde{f}\left(x - \frac{\pi}{2k}, \xi, t\right) \tilde{v}(x, \xi, t)} \left(\frac{1}{u - c} \right)_{\xi \neq y_c} [1 - \alpha(\xi)] \cdot d\xi \quad (2.17) \end{aligned}$$

where $\alpha(\xi)$ is the probability density of the occurrence of the critical layer in the interval $\left(\xi - \frac{1}{2} d\xi, \xi + \frac{1}{2} d\xi\right)$. When Eq. (2.17) is evaluated at $y = 0$ (actually outside the viscous sublayer because the viscosity is ignored), $\tau_w(0)$ should give the momentum transferred to the wave.

2.2 Transformed Wave-Following Coordinate System

It was shown by Hsu, et al. (1977) that the mean flow follows the wave form. Hence, when the critical layer is low as usually encountered in a wave growth period, most of the instantaneous velocity profiles have their critical layer below the wave crests. It is then difficult to collect all the information in a fixed frame. The difficulty of using a fixed frame can be overcome by using a transformed wave-following frame given by

$$\begin{cases} t^* = t \\ x^* = x \\ y^* = y - f\tilde{\eta} \end{cases} \quad (2.18a,b,c)$$

where $\tilde{\eta}$ is the displacement of the wave from mean water level,

$$f(y^*) = \frac{\sinh(kH - ky^*)}{\sinh(kH)} \quad (2.19)$$

and H is the height from the mean water level to the roof of a wind, wave channel. Thus $y^* = 0$ corresponds to the interface $y = \tilde{\eta}$, and $y^* = H$ corresponds to $y = H$, the channel roof. The lines of constant y^* are the streamlines of a potential wave motion in the absence of wind. The adoption of the transformed coordinate system allows a complete description of the flowfield. The difficulty of locating and dealing with an undulating critical layer over the wave form is also nicely circumvented.

In the transformed coordinate system, the wave-induced velocities $\tilde{u}(x^*, y^*)$ and $\tilde{v}(x^*, y^*)$ are regarded as those organized oscillatory velocities around $\bar{u}(y^*)$, which is the mean velocity along a curve

where $y^* = \text{constant}$. The substantial difference between $\tilde{u}(x^*, y^*)$ and $\tilde{u}(x, y)$ was shown by Hsu, et al. (1977). They also showed that $\tilde{u}^*(x^*, y^*)$ and $\tilde{v}^*(x^*, y^*)$ defined by

$$\begin{aligned}\tilde{u}^*(x^*, y^*) &\equiv \tilde{u}(x^*, y^*) - f\tilde{\eta} \frac{\partial \tilde{u}}{\partial y^*} \\ \tilde{v}^*(x^*, y^*) &\equiv \tilde{v}(x^*, y^*)\end{aligned}\tag{2.20a,b}$$

have an equivalent role to $\tilde{u}(x, y)$ and $\tilde{v}(x, y)$.

The difference in the vorticity in the two coordinate systems is noteworthy since the wave-induced vorticity is important in the production of the wave-associated Reynolds stress. The vorticity of the flow is given by

$$\begin{aligned}\Omega &= \frac{\partial u}{\partial y} - \frac{\partial v}{\partial x} \\ &= \frac{\partial \tilde{u}}{\partial y^*} - \frac{\partial f}{\partial y^*} \tilde{\eta} \frac{\partial \tilde{u}}{\partial y^*} - \frac{\partial v}{\partial x^*} + f \frac{\partial \tilde{\eta}}{\partial x} \frac{\partial v}{\partial y^*} + O(k\tilde{\eta})^2\end{aligned}\tag{2.21}$$

Taking a time average (or average along x^*), we have to the first order in $k\tilde{\eta}$

$$\overline{\Omega}(y^*) = \frac{\partial \overline{u}}{\partial y^*}\tag{2.22}$$

Hence, the mean vorticity in the two frames remains the same because the mean velocity \overline{u} in the two frames is the same up to the first order in $k\tilde{\eta}$ (Hsu, et al., 1977). The wave-induced vorticity $\tilde{\Omega}(x^*, y^*)$ measured in (x^*, y^*) is then obtained by subtracting Eq. (2.22) from the phase average of Eq. (2.21) and is

$$\tilde{\Omega}(x^*, y^*) = \frac{\partial \tilde{u}}{\partial y^*} - \frac{\partial f}{\partial y^*} \tilde{\eta} \frac{\partial \overline{u}}{\partial y^*} - \frac{\partial \tilde{v}}{\partial x^*}\tag{2.23}$$

The vorticity $\tilde{\Omega}^*(x^*, y^*)$ is defined by

$$\tilde{\Omega}^*(x^*, y^*) = \frac{\partial \tilde{u}^*}{\partial y^*} - \frac{\partial \tilde{v}^*}{\partial x^*} \quad (2.24)$$

When Eqs. (2.20a,b) and (2.23) are introduced into Eq. (2.24), we find

$$\tilde{\Omega}^*(x^*, y^*) = \tilde{\Omega}(x^*, y^*) - f\tilde{\eta} \frac{\partial \tilde{\Omega}}{\partial y^*} \quad (2.25)$$

which has a form similar to Eq. (2.20a).

The wave-associated Reynolds stress in the transformed coordinate system is now given as

$$\begin{aligned} \tau_w(y^*) &= -\rho \overline{\tilde{u}^* \tilde{v}^*}(y^*) = \rho \int_{y^*}^{\infty} \overline{\tilde{\Omega}^* \tilde{v}^*}(\xi^*) d\xi^* \\ &= \rho \int_{y^*}^{\infty} \overline{\tilde{\Omega} \tilde{v}}(\xi^*) d\xi^* - \rho \int_{y^*}^{\infty} f \cdot \frac{\partial \tilde{\Omega}}{\partial y^*} \overline{\tilde{\eta} \tilde{v}}(\xi^*) d\xi^* \end{aligned} \quad (2.26)$$

We also have

$$\overline{\tilde{u}^* \tilde{v}^*}(y^*) = \overline{\tilde{u} \tilde{v}}(y^*) - f \cdot \frac{\partial \tilde{u}}{\partial y^*} \cdot \overline{\tilde{\eta} \tilde{v}}(y^*) \quad (2.27)$$

At $y^* = 0$, Eq. (2.27) reduces to

$$\overline{\tilde{u}^* \tilde{v}^*}(0) = \overline{\tilde{u} \tilde{v}}(0)$$

because $\overline{\tilde{\eta} \tilde{v}} = 0$ at $y^* = 0$.

3. EXPERIMENTAL APPARATUS AND INSTRUMENTATION

3.1 The Air-Water Channel

The channel used for the experiments was described in detail by Hsu (1965) and subsequent investigators at Stanford. It was designed to facilitate the generation of water waves by wind and/or by a mechanical wave generator for the experimental study of the wave generation problem. Figure 1 shows a schematic of the channel. It is 38 m long, 1 m wide and 1.9 m high. In this study, the distance between the channel roof and the mean water level is 0.97 m. The glass-walled test section is approximately 24 m long, remaining from the air entrance to the down-stream beach. The data taking station was located 13 m from the air entrance.

Wind is produced by drawing air through the test section with a suction fan at the downstream end of the channel. The wind field was conditioned by a thick honeycomb and a group of fine-meshed screens installed at the exit of the air inlet and by a second honeycomb located just in front of the fan. To extend the experiment performed by Hsu, et al. (1977) which was made at a mean free stream velocity, U_{∞} , of 2.4 m/sec, the mean free stream velocities selected in this study were 1.45 and 2.92 m/sec.

The water wave generator is a horizontal-displacement oscillating plate driven by a hydraulic cylinder and subjected to a closed-loop servo-control system. The wave plate is situated well upstream from the entrance of the test section to form a forebay, which acts as a transition region for the development of mechanically-generated water waves. A sloping beach, formed by a series of rectangular baskets

filled with stainless steel turnings, is located at the downstream end of the channel to reduce the wave reflection. The reflected waves amplitudes were less than 5 percent of the incident mechanically-generated wave amplitudes. The frequency of the water wave used in this study was 1 Hz. The wave length determined from the dispersion relation of deep water waves was 1.56 m and the wave number was 4.025 m^{-1} . Hence, the wave speed is 1.56 m/sec which is between the two selected mean free stream velocities.

3.2 Wave-Follower System

The wave-follower system developed by Yu, et al. (1971) and modified by Hsu, et al. (1977) was used as the primary instrument for the measurements. It consists of mechanical and electrical systems and a wave-follower elevator. The mechanical portion contains a low-inertia motor and a vertical motion mechanism that has an aluminum-channel holding a stainless-steel tube guided by nylon bushings. The tube is driven by the motor through a pulley-and-cable assembly. A Pitot-static tube and two x-array hot-film probes separated vertically by 1.2 cm were mounted on a plexiglass frame that was attached to the stainless-steel tube. The electrical portion is a control panel that implements the wave-follower by controlling the motion of the stainless-steel tube. The wave-follower system is mainly controlled by two dials on the control panel: one pre-sets the distance from the mean water level to the probes and the other determines the amplitude of the oscillation of the stainless-steel tube and the attached sensors. The first dial gives the preset distance accurate to $\pm 0.25 \text{ mm}$. The second

dial setting depends on the calibration of a wave height gauge whose output signals was used to guide the wave follower. The wave-follower elevator extends the traverse range of the wave-follower to about 60 cm to cover the whole boundary layer. The elevator was seated on top of the channel roof. The wave-follower was mounted on a moving plate of the elevator with the aluminum channel and the stainless steel tube extending into the wind, wave channel. Figure 2 shows the arrangement of the components.

3.3 Instrumentation and Calibration

The sensors consist of a wave height gauge mounted on an aluminum-angle support fixed to the wind, wave channel roof and the Pitot-static tube and the two x-array hot-film probes attached to the lower end of the wave follower. The arrangement of the measuring probes is shown in Figure 2. Because the wave height signal was used as input for the wave-follower system, the sensing wire of the wave height gauge was installed approximately 4 cm upstream of the other sensors to correct for the phase lag of the wave-follower system. The wave height gauge, the Pitot-static tube, and the two hot-film probes were laterally separated by approximately 5 cm to avoid interference.

The wave height gauge measured the elevation of the instantaneous water surface. The gauge is a capacitance type and is made of No. 32 Nylclad-insulated copper wire stretched between the arms of a U-shaped frame. A complete description of the gauge can be found in Colonell (1966). The calibration of the wave gauge was carried out by mounting the gauge on a vertical traversing mechanism which varied the depth of submergence of the wire in still water. The accuracy of the calibration was ± 0.25 mm. Figure 3 shows the calibration curve.

The Pitot-static tube was used to cross check the mean velocity obtained from the hot-film probes and to calibrate the hot-film probes. The outer diameter of the tube is 2.34 mm. Two leads for the total pressure and the static pressure from the tube were connected to a Pace differential transducer (Model P90D). The Pace transducer was calibrated against a Combust micromanometer, with resolution of 0.006 mm of silicone oil (specific gravity 0.82). Preliminary mean velocity data showed the Pitot-static tube and the hot-film probe results agreed to within 3 percent. Hence, the signal from the Pitot-static tube was not recorded in the final data taking.

The use of two X-array hot-film probes was to measure the instantaneous values of $\partial u / \partial y$ and to obtain the wave-induced flow components. The two hot-film probes were separated vertically by 1.2 cm. Two different probes were used. The upper probe is the (old) probe used by Hsu, et al. (1977) and the lower probe is a mini-probe (TSI Model 1276). The old probe was connected to a TSI 1010A constant temperature anemometer (also used by Hsu, et al.) and the new probe to one port of a set of newly-built anemometers**. This arrangement allows us to cross check the performance of the new hot-film anemometer system. Calibration of the hot-film probes was carried out by locating the probes in the core region of air flow and changing the wind speeds,

** The original plan was to measure the instantaneous velocity profile by using ten miniature probes. Hence, the newly-built anemometers consist of 20 channels of electronic circuitry for ten crossed hot-film probes and the necessary power supplies. Each channel has a constant temperature anemometer, a four-pole butterworth-type low pass filter, a zero offset, and an active amplifier. Unfortunately, the measurement of the instantaneous velocity profiles was not completed due to the termination of this project.

using the Pitot-static tube velocity as a reference. Figure 4 shows the comparison of the typical calibration curves between the old and the new systems. It is seen that the new system has almost the same sensitivity (characterized by the slopes of the curves) as the old system; however, the new system has a lower output than the old system as seen from the output power of the two probes. The hot-film probes were calibrated in situ immediately prior to data taking. The uncertainty in the hot-film probe calibration was mainly caused by the uncertainty in the Pitot-static tube and, hence, was approximately 3 percent.

4. DATA ACQUISITION AND REDUCTION

The wave height and velocity data were taken simultaneously and recorded by a data acquisition-reduction system. The system consists mainly of an HP 2100A computer, an HP 2313 analog-to-digital converter, an HP 7970B nine-track magnetic tape drive and peripheral input-output devices (Takeuchi and Mogel, 1975). All the signals were zero-suppressed, amplified and low-pass filtered at 500 Hz to fulfill the Nyquist criterion as samples were taken every 0.001 seconds for three minutes. The sampled data were stored on digital magnetic tape.

In summary, we have two sets of data at mean free stream wind velocities of 1.4 and 2.9 m/sec. The mechanically-generated water wave frequency is 1 Hz. The amplitudes of the mechanically-generated water waves for the 1.4 and 2.9 m/sec wind speeds were 2.88 and 2.67 cm, respectively. Each run consists of velocity data taken at 30 elevations ranging from 2.0 cm to 41.0 cm above the interface plus the wave height data.

The time average and the phase average defined by (2.4) and (2.5) are the two main schemes used for data reduction. The wave-induced components were then deduced from (2.6). To obtain the amplitude and the phase of the wave-induced components, the wave-induced components deduced from (2.6) were analyzed by a fast-Fourier-transform routine to obtain the cross-spectral density between the wave-induced component and the surface water wave $\tilde{\eta}$. The details of the fast-Fourier-transform routine can be found in Bendat and Piersol (1971, Chapter 9). The detailed data reduction scheme was given in Hsu, et al. (1977).

In deducing the statistical behavior of the instantaneous velocity gradient, the instantaneous velocities of the two probes were reduced first and then the occurrence of the critical layer between the two probes was determined by finding if the velocity of the upper probe is greater than the wave celerity and if the velocity of the lower probe is less than the wave celerity, or vice versa. The probability density $\alpha(y)$ is then obtained by dividing the number of the occurrences of the critical layer between the two probes by the total number of the data examined.

5. EXPERIMENTAL RESULTS

The reduced data consist of those for the mean air flow, the wave-induced flow and the probability distribution $\alpha(y)$. The flow quantities are usually presented in profile distributions as a function of y . Because for a fixed frame, y is a constant and is equal to the average elevation y^* of a transformed wave-following frame at the same data taking station, y is used in abscissa of the figures to be presented below. The profiles are usually in non-dimensional form; U_∞ and U_∞^2 are used to normalize the velocities and the Reynolds stresses, respectively. The abscissa y is then normalized by $1/k$. The wave-induced quantity \tilde{g} is generally expressed as

$$\begin{aligned}\tilde{g} &= \frac{1}{2} [\hat{g} \cdot e^{i(kx-wt)} + \text{conjugate}] + \text{harmonics} \\ &= |\hat{g}| \cdot \cos(kx - wt + \theta_{\tilde{g}}) + \text{harmonics}\end{aligned}$$

where $|\hat{g}|$ is the amplitude and $\theta_{\tilde{g}}$ is the phase lag angle of the fundamental mode. The phase lag is with respect to time using $\tilde{\eta}$ as a reference. In this study, the wave-induced quantity can be approximated by its fundamental mode without changing the overall conclusions, because the harmonics are relatively weak.

5.1 Mean Air Flowfield

The mean wind velocity profiles are shown in Figures 5 and 6 for $U_\infty = 1.45$ and 2.92 m/sec respectively. Agreement between the results obtained by the two probes and in the two coordinate systems is good. This clearly indicates that the mean velocity as observed in the two

frames is not noticeably different. This is the case because as proven by Hsu, et al. (1977) their difference should be to the second order in ka . A wake characteristic near the free stream, as also observed by Hsu, et al. (1977), is evident in the profiles. The friction velocities determined from the profile method are 5.36 and 10.6 cm/sec for $U_\infty = 1.45$ and 2.92 m/sec respectively. Hence, the drag coefficient $u_*^2/U_\infty^2 = 13.0 \cdot 10^{-4}$ which agrees with the value obtained by Hsu, et al. (1977). Figures 7 and 8 show the distributions of the mean turbulent Reynolds stresses. Apparently, $\overline{u'u'}$ is one order in magnitude greater than $-\overline{u'v'}$ and $\overline{v'v'}$. Reasonable agreement between $-\overline{u'v'}/U_\infty^2$ and u_*^2/U_∞^2 is found. The lower $\overline{u_i'u_j}$ for the probe B than that for probe A in Figure 7 may be due to the misalignment of probe B to the flow direction. Because the hot-film sensor in probe B was broken after finishing the first run ($U_\infty/c = 0.93$). The second run ($U_\infty/c = 1.87$) was performed with a new hot-film sensor for probe B. The new probe B has a better alignment with probe A; hence, they produce little difference as shown in Figure 8.

5.2 Wave-Induced Flowfield

For the wave induced flowfield, we will present the data for the wind velocities at 1.45 and 2.92 m/sec separately, because these two sets of data belong to different flow regimes, namely, $U_\infty/c = 0.93 < 1$ and $U_\infty/c = 1.87 > 1$. We will see that the characteristics of the wave-induced flow for these two flow regimes are quite different. This may be because there is no critical layer in the first flow while with higher wind speed a critical layer does exist. The importance of the critical layer is then revealed. We also find that the momentum and energy transfer in the first case is from waves to wind while in the second case is from wind to waves.

5.2a No Critical Layer Case ($U_\infty/c = 0.93 < 1$)

Figures 9 and 10 show the amplitude and phase for the wave-induced velocities u and v respectively. The difference between the results obtained in the fixed frame and the transformed wave-following frame is obvious. While the amplitude $|\hat{u}|$ measured in the fixed frame is considerably greater than that measured in the wave-following frame, the amplitude of \tilde{v} in the fixed frame results is considerably lower than the transformed frame results. The higher \tilde{u} in the fixed frame is apparently due to the behavior of the mean flow which follows the wave form so that the fixed probe picks up a component $f\tilde{\eta}\partial u/\partial y$. However, we find no explanation for the difference between the two frame results in the amplitude $|\hat{v}|$; this phenomena is also observed by Chao, et al. (1976). Further investigations on this aspect is required. The phase $\theta_{\tilde{u}}$ is approximately 180° as expected from the potential flow analysis. The values of $\theta_{\tilde{u}}$ increase to 210° as the interface is approached but have a tendency to return back to 180° near the interface. The phase of $\theta_{\tilde{v}}$ is almost constant at 270° as it should be according to the interface boundary condition. In general, the wave-induced flow at this wind speed is similar to the flow inferred from a potential flow analysis, with minor modification on the amplitude distribution by turbulence. Again, the deviation between the results obtained by probes A and B in Figure 10(a) may be due to the misalignment of probe B.

Figure 11 shows the wave-associated Reynolds stress $-\overline{\tilde{u}\tilde{v}}$ versus ky . Near the interface (but outside a viscous Stokes layer), the wave-associated Reynolds stress is negative. This means that the momentum and energy transfer is from the waves to the wind. That is that the

wind is lagging behind the propagation of the waves so as to drag on the waves and result in their attenuation. In Section 2.2, we have shown that the values of $-\overline{\tilde{u}\tilde{v}}$ measured in the two frames should differ by $f\partial\bar{u}/\partial y \cdot \tilde{\eta}\tilde{v}$. Since $\tilde{\eta}$ and \tilde{v} are almost 90° out of phase, $\overline{\tilde{\eta}\tilde{v}}$ is probably very small. As a result, no significant difference in $-\overline{\tilde{u}\tilde{v}}$ between the two frames is found in Figure 11.

Figures 12, 13 and 14 show the amplitudes and phases for the wave-induced turbulent Reynolds stresses as functions of ky . Hsu, et al. (1978) showed that \tilde{r}_{11} is approximately twice \tilde{r}_{12} and is one order of magnitude greater than \tilde{r}_{22} near the interface. This is the situation for \tilde{r}_{11} , \tilde{r}_{12} and \tilde{r}_{22} shown in Figures 12, 13 and 14. In these figures we also find no phase jump associated with the phase distributions of $\theta_{\tilde{r}_{11}}$, $\theta_{\tilde{r}_{12}}$ and $\theta_{\tilde{r}_{22}}$. This is different from what was observed by Hsu, et al. (1977) for $U_\infty/c = 1.57$ where a consistent phase jump at $ky = 0.6$ was evident in their figures for $\theta_{\tilde{r}_{11}}$, $\theta_{\tilde{r}_{12}}$, and $\theta_{\tilde{r}_{22}}$. Hence, it is felt that the structure of the wave-induced flow for the no-critical-layer case is different from that with a critical layer.

The data in general agree with those obtained by Chao, et al. (1976). The present data is more complete than theirs because the wave-following measurement in this study covers the whole boundary layer except in the immediate vicinity of the interface.

5.2b Critical Layer Flow (Low Critical Layer, $U_\infty/c = 1.87 > 1$)

Figures 15 and 16 show the amplitude and phase for the wave-induced velocities \tilde{u} and \tilde{v} , respectively, for $U_\infty/c = 1.87$. As shown in Figure 15a, the amplitude $|\hat{u}|$ measured in the fixed frame is smaller than that measured in the transformed wave-following frame. This is

opposite to what we observed for the no critical layer case. This reversal is also found in the amplitude distribution of $|\hat{v}|$ shown in Figure 16. The measurement by Hsu, et al. (1977) indicated that the phase $\theta_{\tilde{u}}$ tends to be 90° and that the phase $\theta_{\tilde{v}}$ tends to be 270° near the interface. Figures 15 and 16 clearly show this tendency; however, the variation in $\theta_{\tilde{u}}$ and $\theta_{\tilde{v}}$ at this higher wind speed is so rapid that our measurement does not reach close enough to the interface to reveal accurately the phase angles at the interface.

The distributions of $-\overline{\tilde{u}\tilde{v}}$ are shown in Figure 17. They have a trend similar to those measured by Hsu, et al. (1977) and by Kendall (1970). In Hsu, et al. (1977), they observed a rapidly increasing region of positive values of $-\overline{\tilde{u}\tilde{v}}$ as one approaches the interface. Such a region was not measured here because it is too close to the interface at this wind speed for our probe to reach. The measurement by Kendall (1970) indicated that this characteristic could not be detected with a fixed probe even at lower wind speeds. However, a tendency toward a positive value in $-\overline{\tilde{u}\tilde{v}}$ when approaching the interface is seen in Figure 17, as in the data of Kendall (1970). The difference in the measured value of $-\overline{\tilde{u}\tilde{v}}(y)$ and $-\overline{\tilde{u}\tilde{v}}(y^*)$ is the value of $f \frac{\partial U}{\partial y^*} \tilde{\eta} \tilde{v}$ is positive because $\frac{\partial U}{\partial y^*} > 0$. Hence, $-\overline{\tilde{u}\tilde{v}}(y) > -\overline{\tilde{u}\tilde{v}}(y^*)$. This feature is apparent in Figure 17.

Figures 18, 19 and 20 show the amplitudes and phases for r_{ij} as functions of k_y at this wind speed. The phase jump of 180° at the elevation of approximately $k_y = 0.4$ is clear for all the three components of $\theta_{\tilde{r}_{11}}$, $\theta_{\tilde{r}_{12}}$ and $\theta_{\tilde{r}_{22}}$. This is consistent with the measurement by Hsu, et al. (1977). Hence, we also expect that the amplitude of \tilde{r}_{ij} should have a minimum of zero at approximately $k_y = 0.4$ as a

consequence of this stress reversal there. The amplitudes of \tilde{r}_{ij} are in good agreement with those predicted by Hsu, et al. (1978), i.e., near the interface, we have $\tilde{r}_{11} \approx 2\overline{u'u'}k\tilde{\eta}$, $\tilde{r}_{12} \approx \overline{u'u'}\partial\tilde{\eta}/\partial x$ and $\tilde{r}_{22} \approx 2\overline{u'v'}\partial\tilde{\eta}/\partial x$. Since the characteristics of \tilde{r}_{11} at this wind speed are similar to those measured by Hsu, et al. (1977) for $U_\infty/c = 1.57$, the reader is referred to Hsu, et al. (1977) for details of the structure of \tilde{r}_{ij} .

5.3 Probability Distribution $\alpha(y)$

Table 1 shows the result of the joint probability between the u values measured by the two probes for $U_\infty = 1.45$ m/sec. It is seen that the most probable occurrence is in the case $\{u_a < c \text{ and } u_b < c\}$ where u_a is the horizontal instantaneous velocity measured by the old probe (higher elevation) and u_b is that measured by the new probe (lower elevation). This higher occurrence for $\{u_a < c \text{ and } u_b < c\}$ is expected because the mean velocity \bar{u} is always less than c . However, the case $\{u_a > c \text{ and } u_b < c\}$, which is favorable for evaluating the momentum and energy transfer from wind to waves according to the modified Miles' theory, happens more frequently than the remaining two cases. For $U_\infty < c$, there is no critical layer according to Miles' theory. But, near the free stream, turbulent fluctuation tends to produce an instantaneous velocity profile with u greater than c at the outer edge of the boundary layer where the flow is strongly intermittent.

Table 2 shows the joint probability result for the case of $U_{\infty} = 2.92$ m/sec. Now, the case $\{u_a > c \text{ and } u_b > c\}$ is the most probable case because the measured \bar{u} at each elevation is much higher than c . Although at this wind speed ($U_{\infty} > c$) is different from the previous one ($U_{\infty} < c$), the favorable case of $\{u_a > c \text{ and } u_b < c\}$ is still higher than the remaining two cases. If we include the turbulent effect and regard the statistical result of this time-varying critical layer as a turbulently-mixed critical layer, we see that turbulence tends to move the mean location of the critical layer toward the location where the turbulence has its highest intensity.

6. CONCLUDING REMARKS

This study provides a first insight into the difference between the wave-induced flow quantities measured in fixed and wave-following-transformed reference frames. The two measured wind speeds cover two different flow regimes with $U_\infty < c$ and $U_\infty > c$. The wave-induced flow for these two flow regimes has different characteristics. The phase jump for \tilde{r}_{ij} when $U_\infty > c$ may be crucial in the wave generation process by the wind. It is felt that the two wind speeds used in this study were not very efficient in defining the instantaneous critical layer relevant to the modified Miles' theory. For a better result, a wind speed U_∞ just above the wave celerity should be used.

REFERENCES

- Barnett, T. P. and J. C. Wilkerson (1976), "On the Generation of Ocean Wind Waves as Inferred from Airborne Radar Measurements of Fetch-Limited Spectra," J. Mar. Res., 25(3), pp. 292-321.
- Bendat, J. S. and A. G. Piersol (1971), Random Data: Analysis and Measurement Procedures, Wiley-Interscience, New York.
- Benjamin, T. B. (1959), "Shearing Flow over a Wavy Boundary," J. Fluid Mech., Vol. 6, pp. 161-205
- Bole, J. B. and E. Y. Hsu (1969), "Response of gravity water waves to wind excitation," J. Fluid Mech., 35, pp. 657-675.
- Chao, S. P., E. Y. Hsu and R. L. Street (1976), "The interaction between turbulent wind and progressive water waves," Tech. Rept. No. 204, Dept. of Civil Engr., Stanford Univ., Stanford, Calif.
- Colonell, J. M. (1966), "Laboratory Simulation of Sea Waves," Dept. of Civil Engr., Tech. Rept. No. 65, Stanford University, Stanford, California.
- Davis, R. E. (1969), "On the high Reynolds number flow over a wavy boundary," J. Fluid Mech., 36, p. 337.
- Davis, R. E. (1970), "On the Turbulent Flow over a Wavy Boundary," J. Fluid Mech., 42(5), pp. 721-731.
- Davis, R. E. (1972), "On Prediction of the Turbulent Flow over a Wavy Boundary," J. Fluid Mech., 52(2), pp. 287-306.
- Davis, R. E. (1974), "Perturbed Turbulent Flow, Eddy Viscosity and the Generation of Turbulent Stresses," J. Fluid Mech., Vol. 63, Part 4, pp. 673-693.
- Dobson, R. W. (1971), "Measurements of Atmospheric Pressure on Wind-Generated Sea Waves," J. Fluid Mech., Vol. 48, Part 1, pp. 91-127.
- Gent, P. R. and P. A. Taylor (1976), "A Numerical Model of the Air Flow above Water Waves," J. Fluid Mech., Vol. 77, pp. 105-128.
- Hasselmann, K. (1968), "Weak Interaction Theory of Ocean Waves," Basic Developments in Fluid Dynamics, Vol. 2, Ed. by M. Holt. Academic Press, New York.
- Hsu, E. Y. (1965), "A wind, water-wave research facility," Dept. of Civil Engr. Tech. Rept. No. 57, Stanford Univ., Stanford, Calif.

- Hsu, C. T., E. Y. Hsu and R. L. Street (1977), "The Structure of Modulated Turbulent Flow Over Progressive Water Waves," Dept. of Civil Engr., Tech. Rept. No. 221, Stanford University, Stanford, California.
- Hsu, C. T., E. Y. Hsu and R. L. Street (1978), "On the Structure of Turbulent Flow over a Progressive Water Wave. Part I. Theoretical Aspects of Flow Structure in a Transformed Coordinate System; Momentum and Energy Transfer Across the Interface," submitted for publication.
- Kendall, J. M. (1970), "The Turbulent Boundary Layer over a Wall with Progressive Surface Waves," J. Fluid Mech., Vol. 41, pp. 259-281.
- Kim, H. T., S. J. Kline and W. C. Reynolds (1971), "The Production of Turbulence near a Smooth Wall in a Turbulent Boundary Layer," J. Fluid Mech., 50, pp. 133-160.
- Lightill, M. J. (1962), "Physical Interpretation of the Mathematical Theory of Wave Generation by Wind," J. Fluid Mech., 14, pp. 385-398.
- Long, R. B. (1971), "On Generation of Ocean Waves by a Turbulent Wind," Ph.D. Dissertation, University of Miami, Coral Gables, Florida.
- Miles, J. W. (1957), "On the Generation of Surface Waves by Shear Flows," J. Fluid Mech., Vol. 3, pp. 185.
- Miles, J. W. (1959), "On the Generation of Surface Waves by Shear Flows. Part 2," J. Fluid Mech., Vol. 6, Part 4, pp. 568-582.
- Norris, H. L. and Reynolds, W. C. (1975), "Turbulent Channel Flow with a Moving Wavy Boundary," Mech. Engrg. Dept., Report TF-7, Stanford, University.
- Phillips, O. M. (1957), "On the Generation of Surface Waves by Turbulent Wind," J. Fluid Mech., Vol. 2, pp. 417-445.
- Saeger, J. C. and Reynolds, W. C. (1971), "Perturbation Pressures Over Traveling Sinusoidal Waves with Fully Developed Turbulent Shear Flow," Mech. Engrg. Dept., Report No. FM-9, Stanford University.
- Snyder, R. L. and C. S. Cox (1966), "A field study of the wind generation of ocean waves," J. Mar. Res., 24(2), pp. 141-178.
- Stewart, R. H. (1970), "Laboratory Studies of the Velocity Field Over Deep-Water Waves," J. Fluid Mech., Vol. 42, Part 4, pp. 733-754.
- Stewart, R. W. (1967), "Mechanics of air-sea interface," Phys. Fluids Suppl., 10, pp. S47-55.
- Stewart, R. W. (1974), "The Air-Sea Momentum Exchange," Boundary-Layer Meteorol., 6, pp. 151-167.

- Takeuchi, K. and Mogel, T. R. (1975), "A Performance Evaluation of a Mini-Computer," Rev. Sci. Instrum., Vol. 46, No. 6, pp. 686-691.
- Townsend, A. A. (1972), "Flow in a Deep Turbulent Boundary Layer Over a Surface Distorted by Water Waves," J. Fluid Mech., 55, pp. 719-753.
- Yu, H. Y., Hsu, E. Y. and Street, R. L. (1971), "A Refined Measurement of Aerodynamic Pressure Over Progressive Water Waves," Civil Engrg. Dept., Report No. 146, Stanford University.
- Yu, H. Y., E. Y. Hsu and R. L. Street (1973), "Wave-induced perturbations in a turbulent boundary layer over progressive water waves," Dept. of Civil Engr. Tech. Rept. No. 172, Stanford Univ., Stanford, Calif.

TABLE 1

Probability for the Occurrence of Critical Layers Above the Interface
($U_{\infty}/c = 0.93$)

A. Wave-Following Coordinate System

y (cm)	No. of $\begin{pmatrix} u_a < c \\ u_b < c \end{pmatrix}$	No. of $\begin{pmatrix} u_a < c \\ u_b \geq c \end{pmatrix}$	No. of $\begin{pmatrix} u_a \geq c \\ u_b < c \end{pmatrix}$	No. of $\begin{pmatrix} u_a \geq c \\ u_b \geq c \end{pmatrix}$	$\alpha(y) \times 10^2$
2.6035	184320	0	0	0	0
3.1115	184320	0	0	0	0
3.8735	184320	0	0	0	0
4.8895	184316	0	4	0	0.0022
6.1595	184310	0	10	0	0.0054
7.4295	184301	0	19	0	0.0103
8.6995	184306	0	14	0	0.0076
10.6045	184266	0	54	0	0.0293
12.5095	184206	0	114	0	0.0618
15.0495	183876	0	444	0	0.2409
17.5895	183072	1	1244	3	0.6771
21.3995	182020	1	2296	3	1.2478
26.4795	181727	2	2590	1	1.4068
32.8295	181431	0	2872	17	1.5674
40.4495	184257	0	63	0	0.0342

B. Fixed Coordinate System

y (cm)	No. of $\begin{pmatrix} u_a < c \\ u_b < c \end{pmatrix}$	No. of $\begin{pmatrix} u_a < c \\ u_b \geq c \end{pmatrix}$	No. of $\begin{pmatrix} u_a \geq c \\ u_b < c \end{pmatrix}$	No. of $\begin{pmatrix} u_a \geq c \\ u_b \geq c \end{pmatrix}$	$\alpha(y) \times 10^2$
2.6038	--	--	--	--	--
3.1115	--	--	--	--	--
3.8735	--	--	--	--	--
4.8895	184320	0	0	0	0
6.1595	184320	0	0	0	0
7.4295	184312	0	8	0	0.0043
8.6995	184293	0	27	0	0.0146
10.6045	184229	0	91	0	0.0494
12.5095	184276	0	44	0	0.0239
15.0495	184159	0	161	0	0.0873
17.5895	183949	2	367	2	0.2013
21.3995	183286	10	1021	3	0.5610
26.4795	183981	0	332	7	0.1839
32.8295	183977	0	336	7	0.1861
40.4495	184319	0	1	0	0.0005

TABLE 2

Probability for the Occurrence of Critical Layers Above the Interface
($U_{\infty}/c = 1.87$)

A. Wave-Following Coordinate System

y (cm)	No. of $\begin{pmatrix} u_a < c \\ u_b < c \end{pmatrix}$	No. of $\begin{pmatrix} u_a < c \\ u_b \geq c \end{pmatrix}$	No. of $\begin{pmatrix} u_a \geq c \\ u_b < c \end{pmatrix}$	No. of $\begin{pmatrix} u_a \geq c \\ u_b \geq c \end{pmatrix}$	$\alpha(y) \times 10^2$
2.6035	326	499	2009	181486	1.3607
3.1115	106	381	1017	182816	0.7585
3.8735	39	144	492	183645	0.3450
4.8895	5	77	88	184150	0.0895
6.1595	0	0	8	184312	0.0043
7.4295	0	2	6	184312	0.0043
8.6995	0	0	0	184320	0

B. Fixed Coordinate System

y (cm)	No. of $\begin{pmatrix} u_a < c \\ u_b < c \end{pmatrix}$	No. of $\begin{pmatrix} u_a < c \\ u_b \geq c \end{pmatrix}$	No. of $\begin{pmatrix} u_a \geq c \\ u_b < c \end{pmatrix}$	No. of $\begin{pmatrix} u_a \geq c \\ u_b \geq c \end{pmatrix}$	$\alpha(y) \times 10^2$
2.6035	--	--	--	--	--
3.1115	--	--	--	--	--
3.8735	--	--	--	--	--
4.8895	6	32	113	184169	0.0787
6.1595	4	1	3	184312	0.0022
7.4295	0	0	0	184320	0

$\alpha(y)$ = Probability of [$u_a < c$, $u_b \geq c$] or [$u_a \geq c$, $u_b < c$]

Total data no. = 184320.

"--" means that it cannot be measured.

LIST OF FIGURES

- Figure 1. Schematic of Stanford Wind, Water-Wave Facility.
- Figure 2. Probe Configurations.
- Figure 3. Calibration Curve of Wave Height Gauge.
- Figure 4. Typical Calibration Curves for the Hot-Film Probes,
A1, A2 -- Films 1 and 2 of Probe No. A (Old Probe),
B1, B2 -- Films 1 and 2 of Probe No. B (New Probe).
- Figure 5. Mean Velocity Profiles for $U_{\infty}/c = 0.93$.
- Figure 6. Mean Velocity Profiles for $U_{\infty}/c = 1.87$.
- Figure 7. Profiles for Mean Turbulent Reynolds Stresses ($U_{\infty}/c = 0.93$).
- Figure 8. Profiles for Mean Turbulent Reynolds Stresses ($U_{\infty}/c = 1.87$).
- Figure 9. Amplitude and Phase Distributions for \tilde{u} at $U_{\infty}/c = 0.93$.
- Figure 10. Amplitude and Phase Distributions for \tilde{v} at $U_{\infty}/c = 0.93$.
- Figure 11. Distributions of the Wave-Associated Reynolds Stress $-\overline{\tilde{u}\tilde{v}}$.
($U_{\infty}/c = 0.93$)
- Figure 12. Amplitude and Phase Distributions for \tilde{r}_{11} at $U_{\infty}/c = 0.93$.
- Figure 13. Amplitude and Phase Distributions for \tilde{r}_{12} at $U_{\infty}/c = 0.93$.
- Figure 14. Amplitude and Phase Distributions for \tilde{r}_{22} at $U_{\infty}/c = 0.93$.

- Figure 15. Amplitude and Phase Distributions for \tilde{u} at $U_{\infty}/c = 1.87$.
- Figure 16. Amplitude and Phase Distributions for \tilde{v} at $U_{\infty}/c = 1.87$.
- Figure 17. Distribution of the Wave-Associated Reynolds Stresses $-\overline{\tilde{u}\tilde{v}}$.
($U_{\infty}/c = 1.87$)
- Figure 18. Amplitude and Phase Distributions for \tilde{r}_{11} at $U_{\infty}/c = 1.87$.
- Figure 19. Amplitude and Phase Distributions for \tilde{r}_{12} at $U_{\infty}/c = 1.87$.
- Figure 20. Amplitude and Phase Distributions for \tilde{r}_{22} at $U_{\infty}/c = 1.87$.

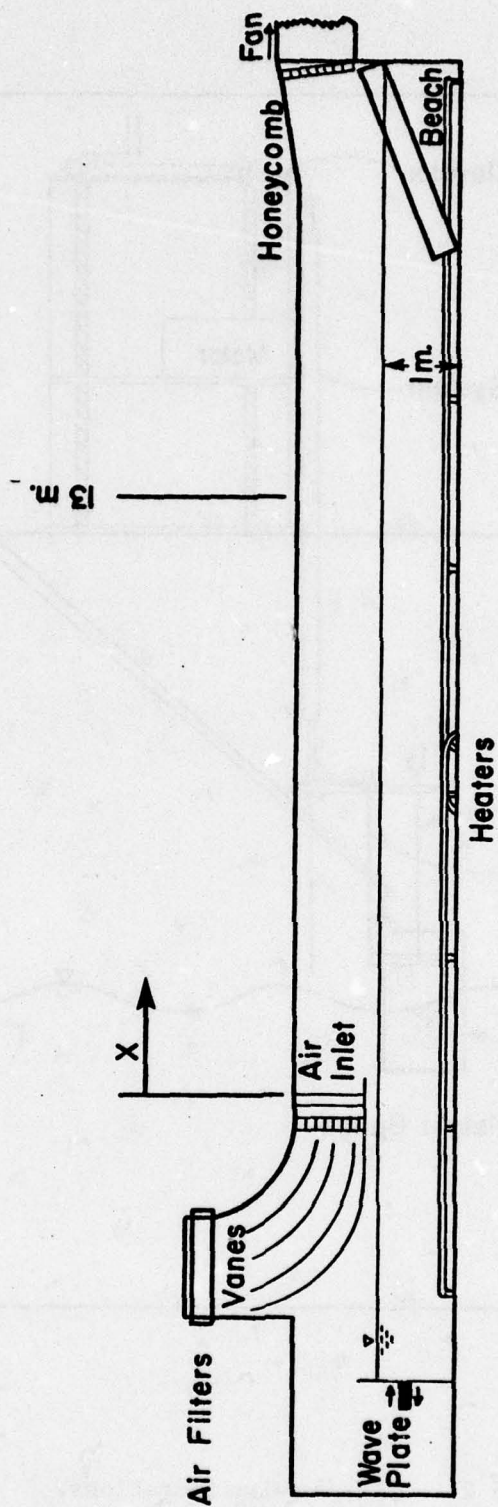


Figure 1. Schematic of Stanford Wind, Water-Wave Facility.

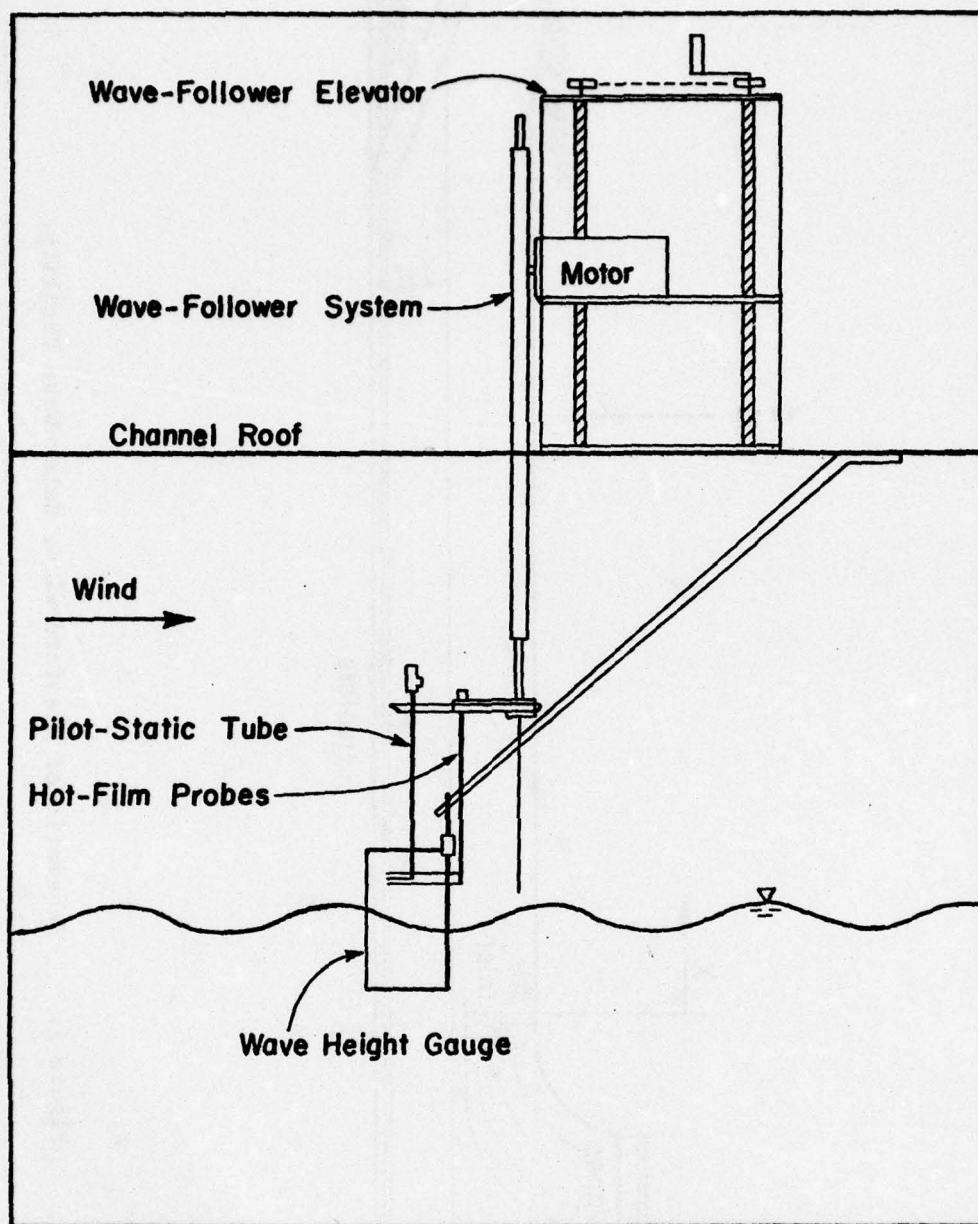


Figure 2. Probe Configurations.

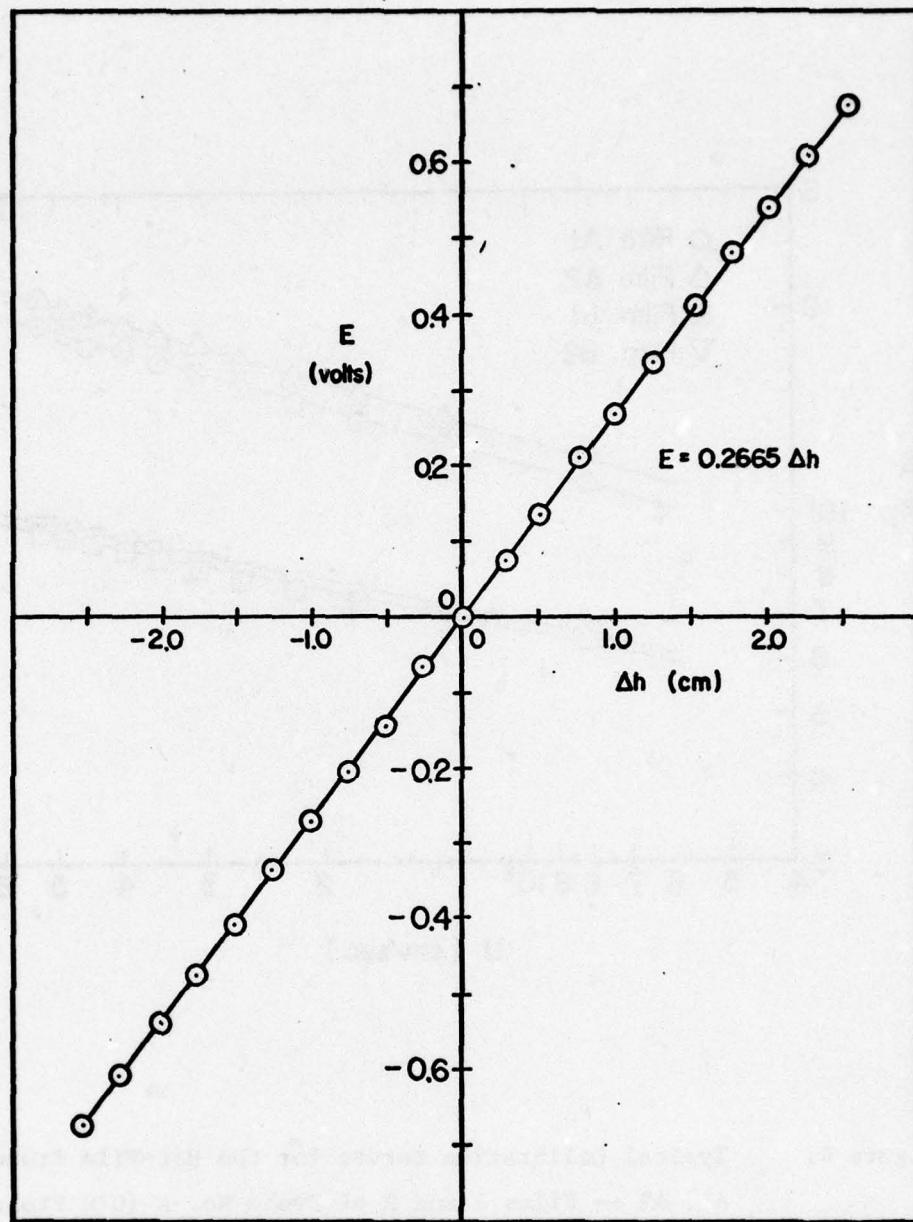


Figure 3. Calibration Curve of Wave Height Gauge.

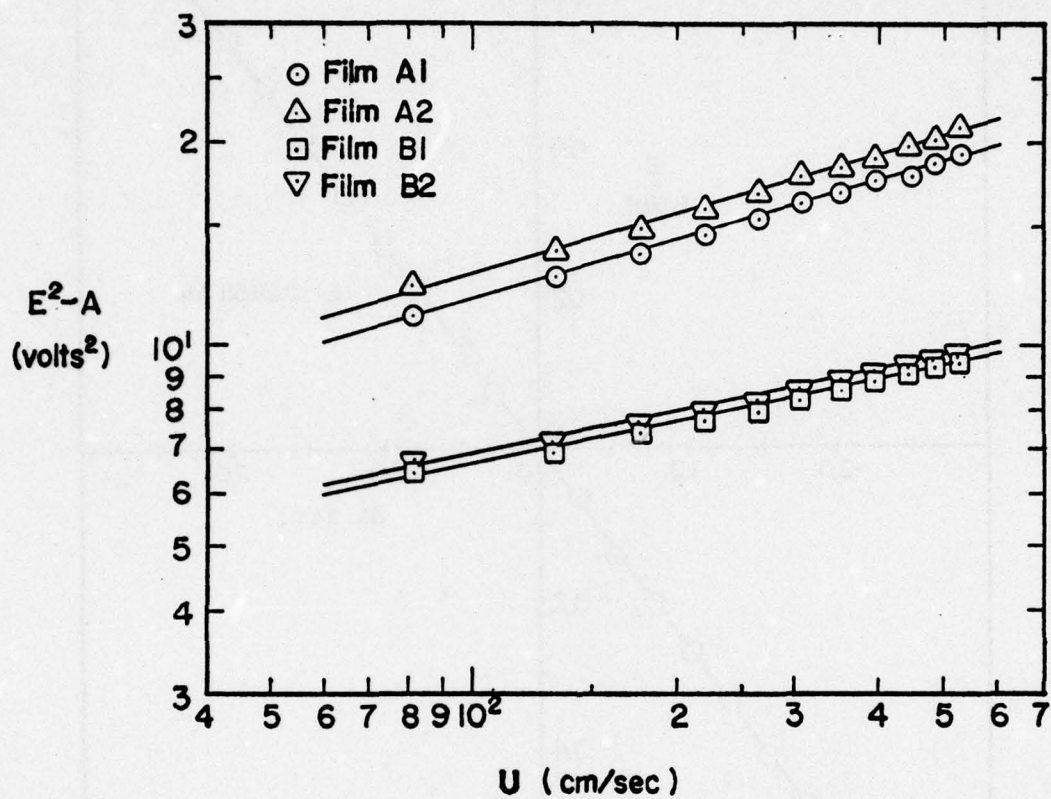


Figure 4. Typical Calibration Curves for the Hot-Film Probes, A1, A2 -- Films 1 and 2 of Probe No. A (Old Probe), B1, B2 -- Films 1 and 2 of Probe No. B (New Probe).

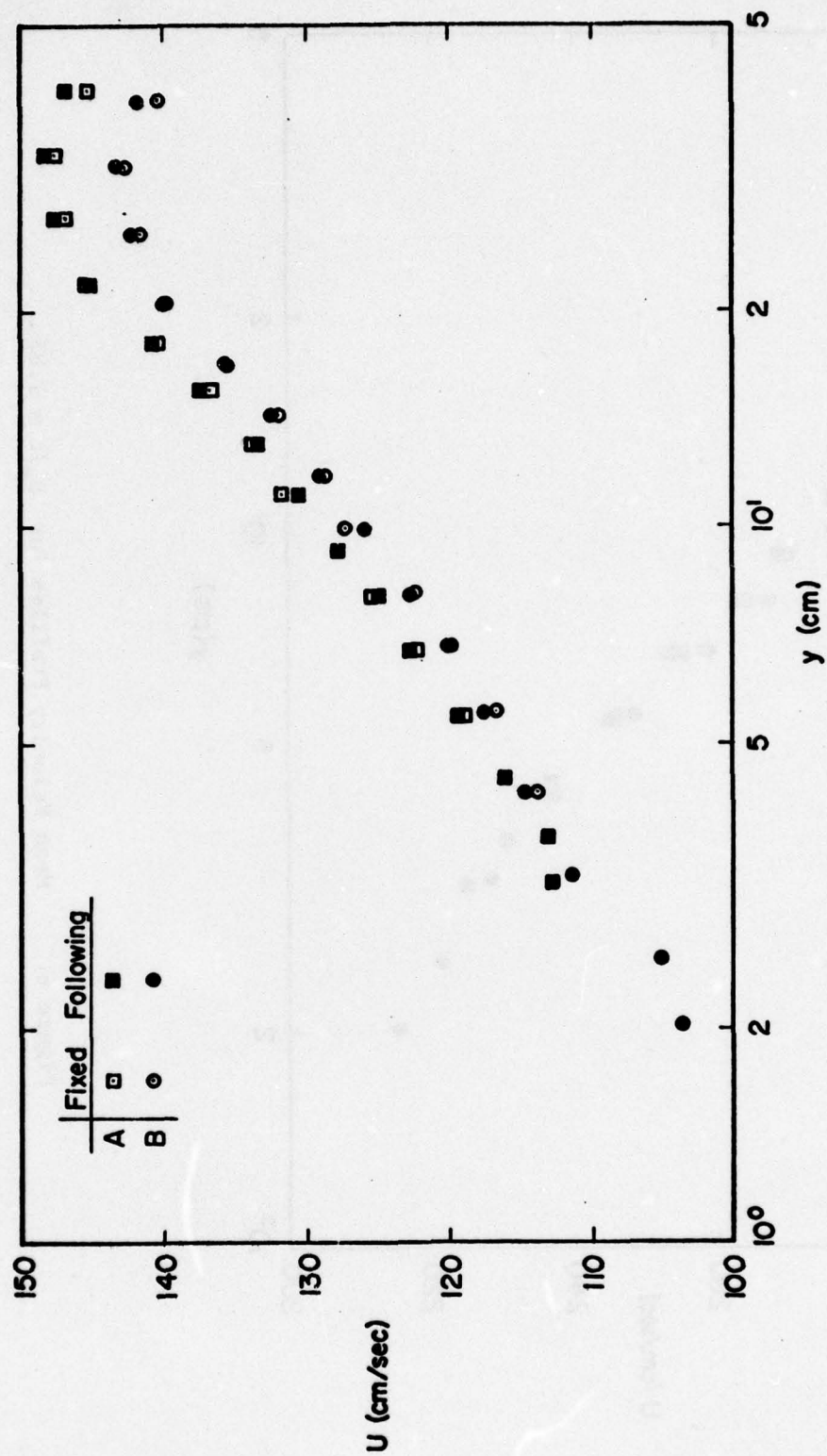


Figure 5. Mean Velocity Profiles for $U_{\infty}/c = 0.93$.

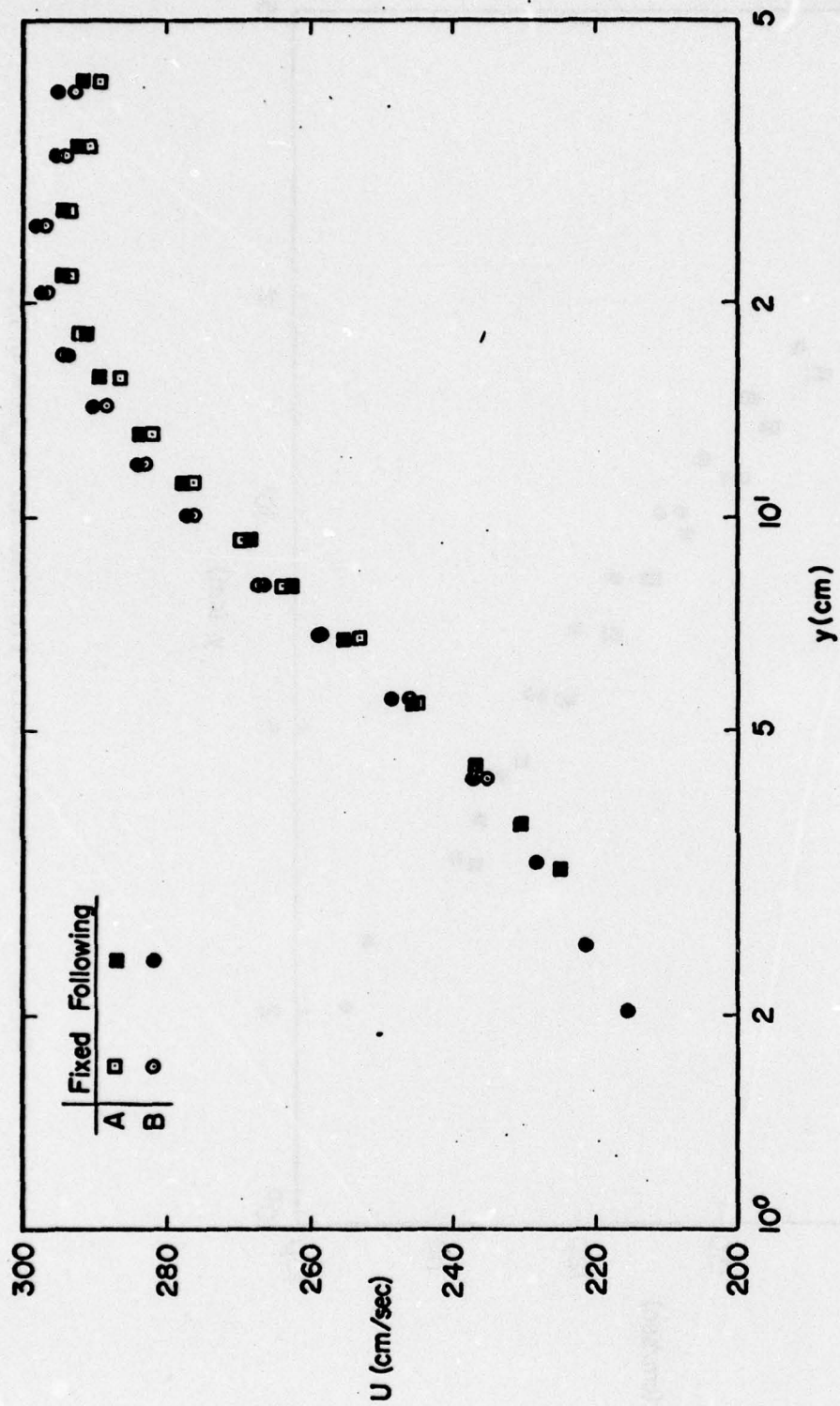


Figure 6. Mean Velocity Profiles for $U_\infty/c = 1.87$.

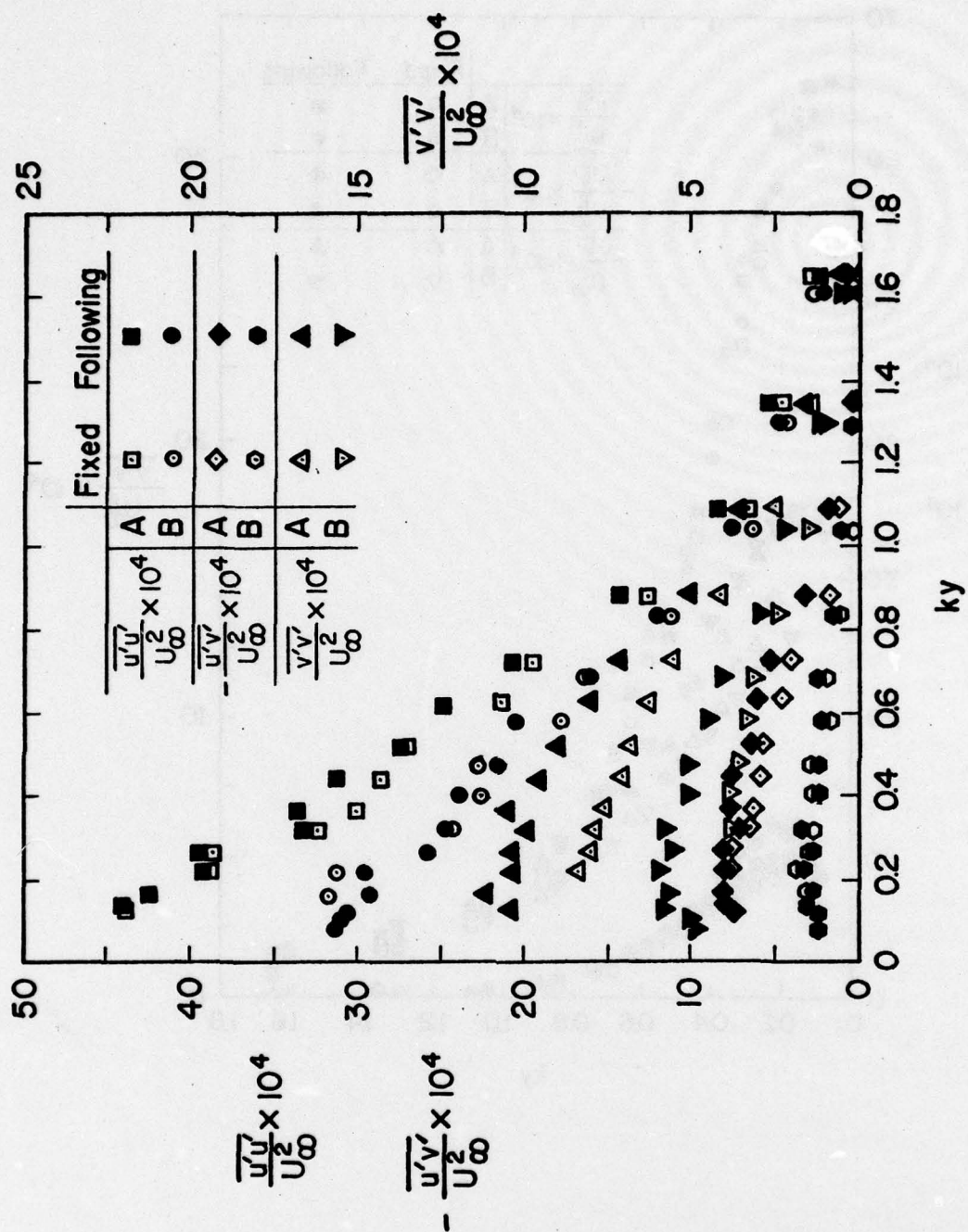


Figure 7. Profiles for Mean Turbulent Reynolds Stresses ($U_\infty/c = 0.93$).

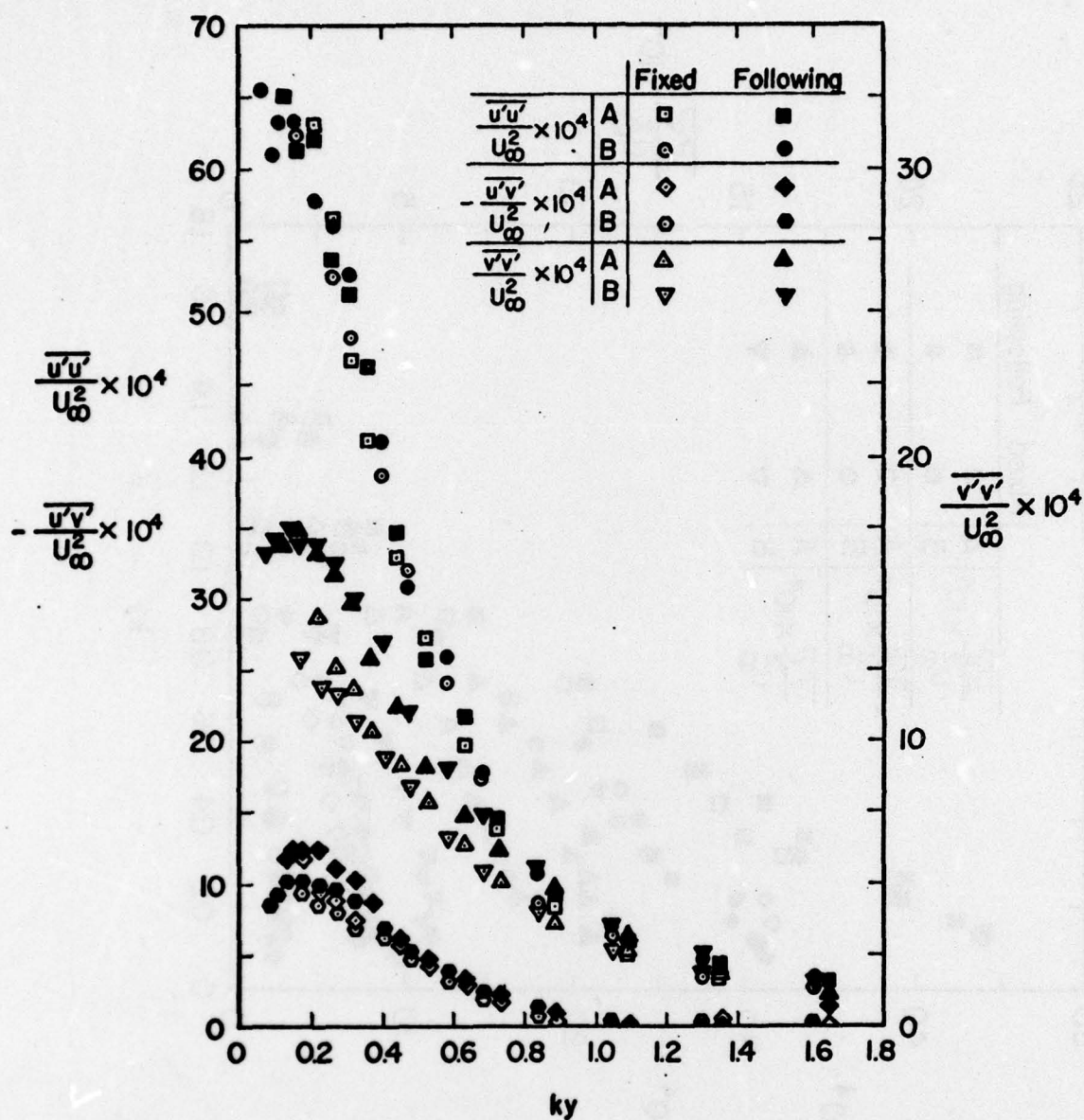


Figure 8. Profiles for Mean Turbulent Reynolds Stresses ($U_\infty/c = 1.87$).

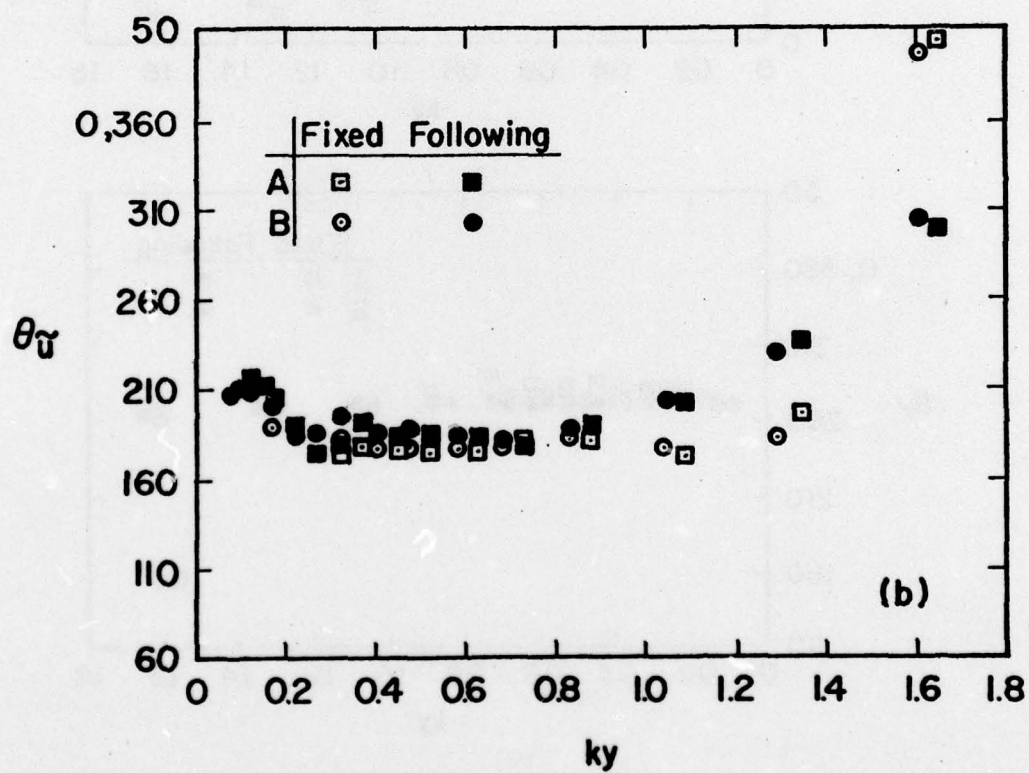
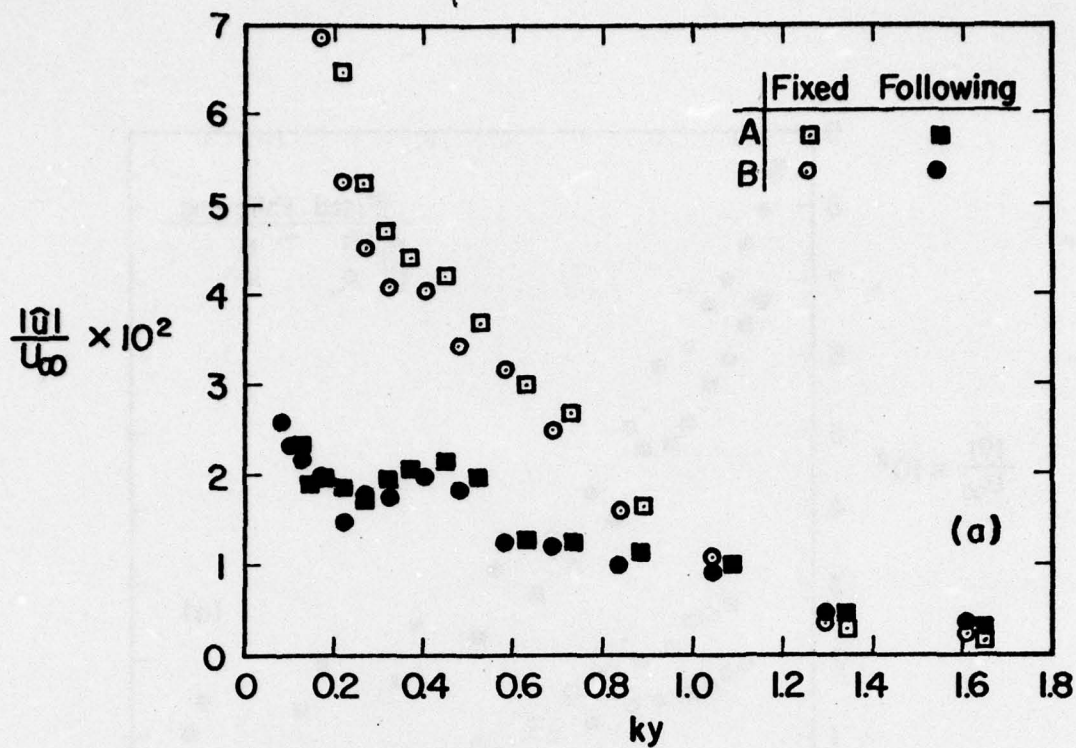


Figure 9. Amplitude and Phase Distributions for \tilde{u} at $U_\infty/c = 0.93$.

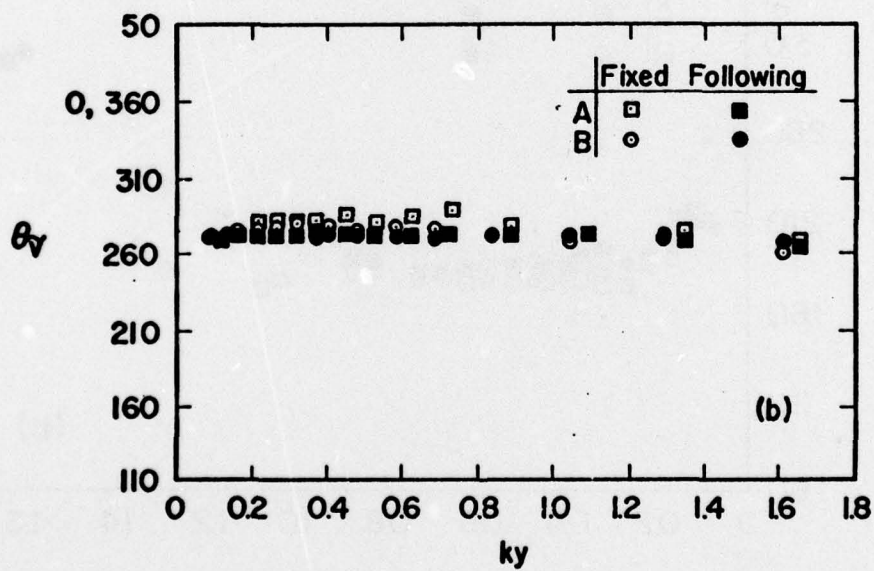
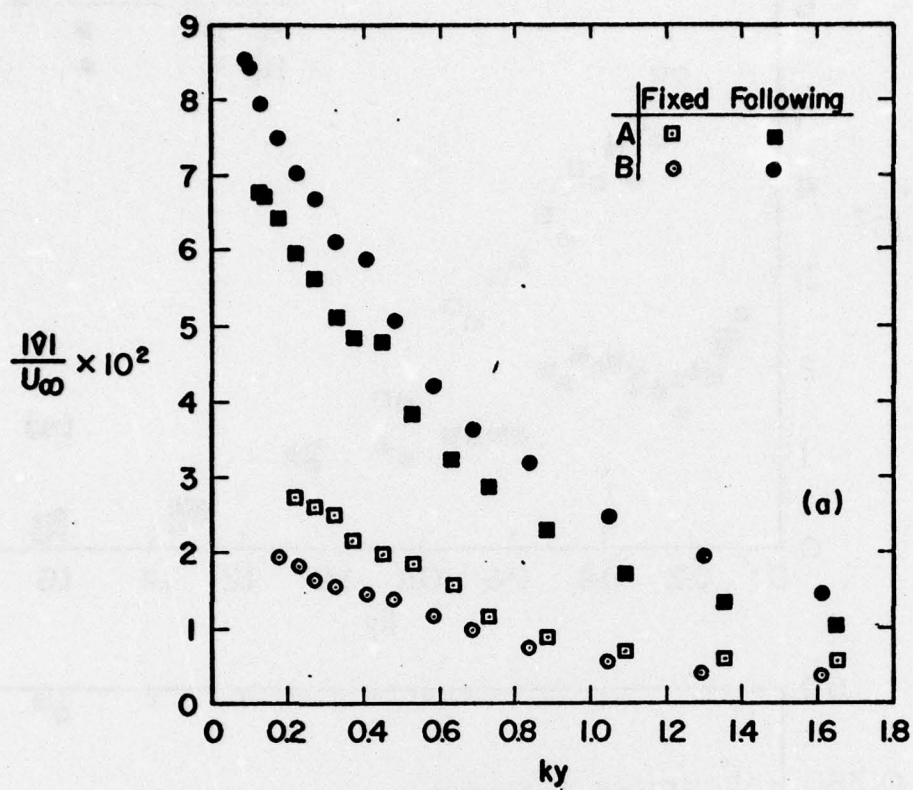


Figure 10. Amplitude and Phase Distributions for \tilde{v} at $U_\infty/c = 0.93$.

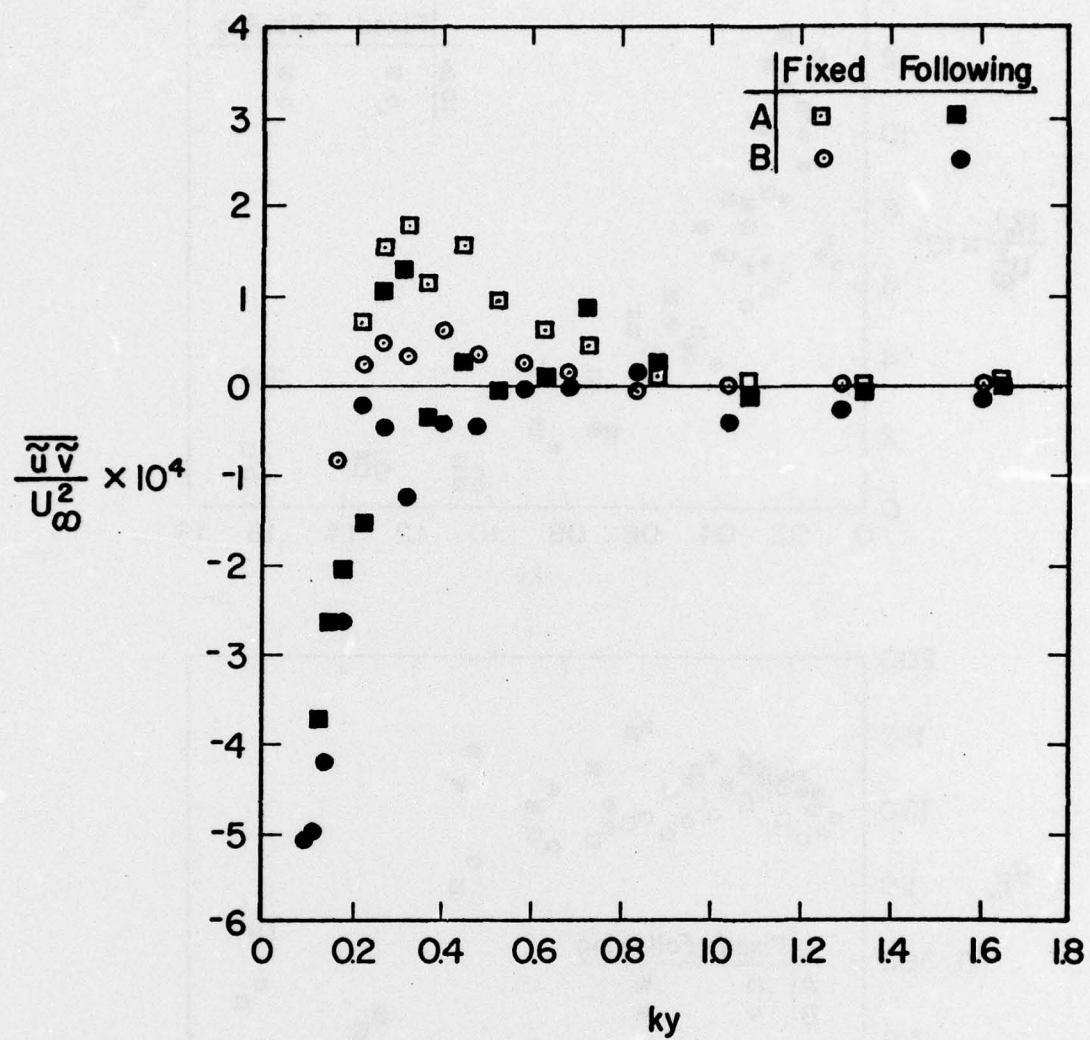


Figure 11. Distributions of the Wave-Associated Reynolds Stress $-\overline{\tilde{u}\tilde{v}}$.
 $(U_\infty/c = 0.93)$

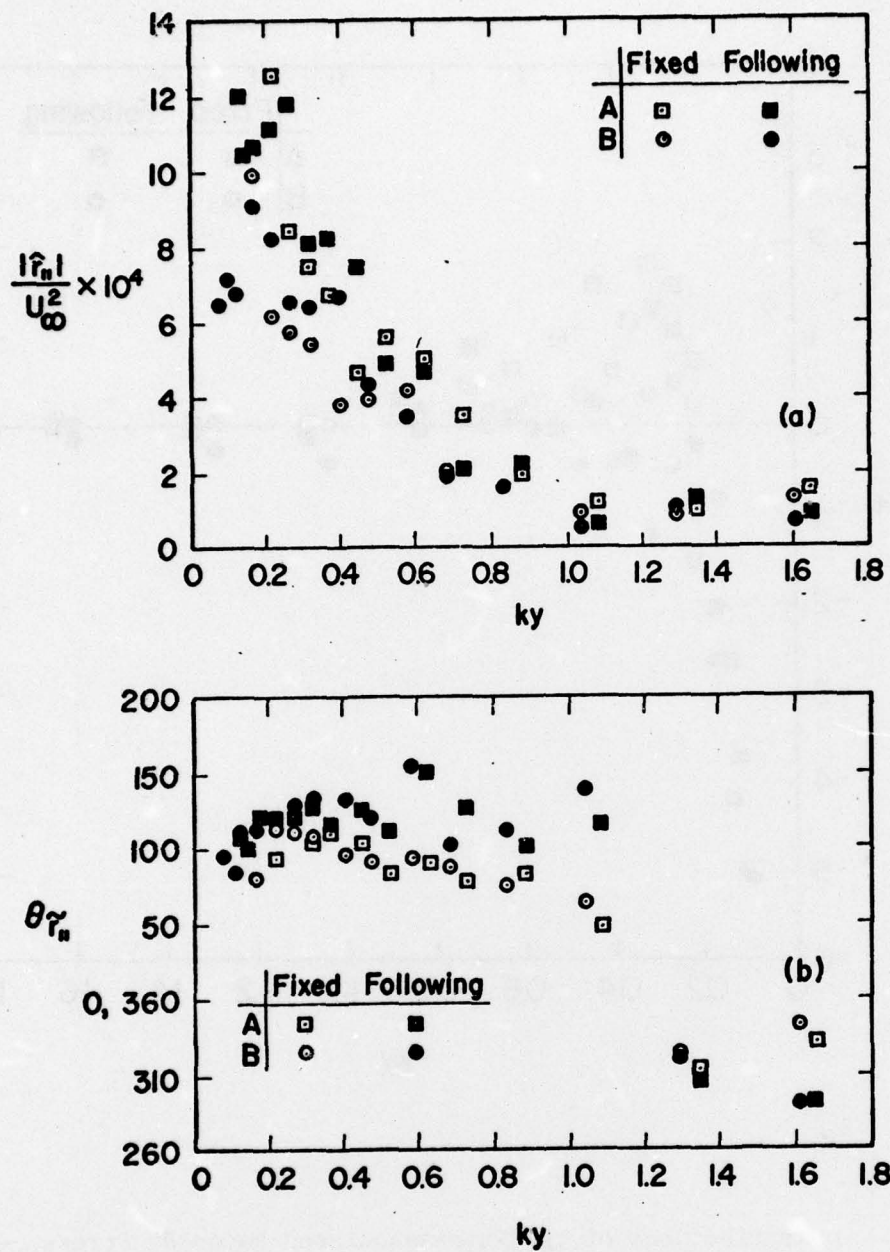


Figure 12. Amplitude and Phase Distributions for \tilde{r}_{11} at $U_\infty/c = 0.93$.

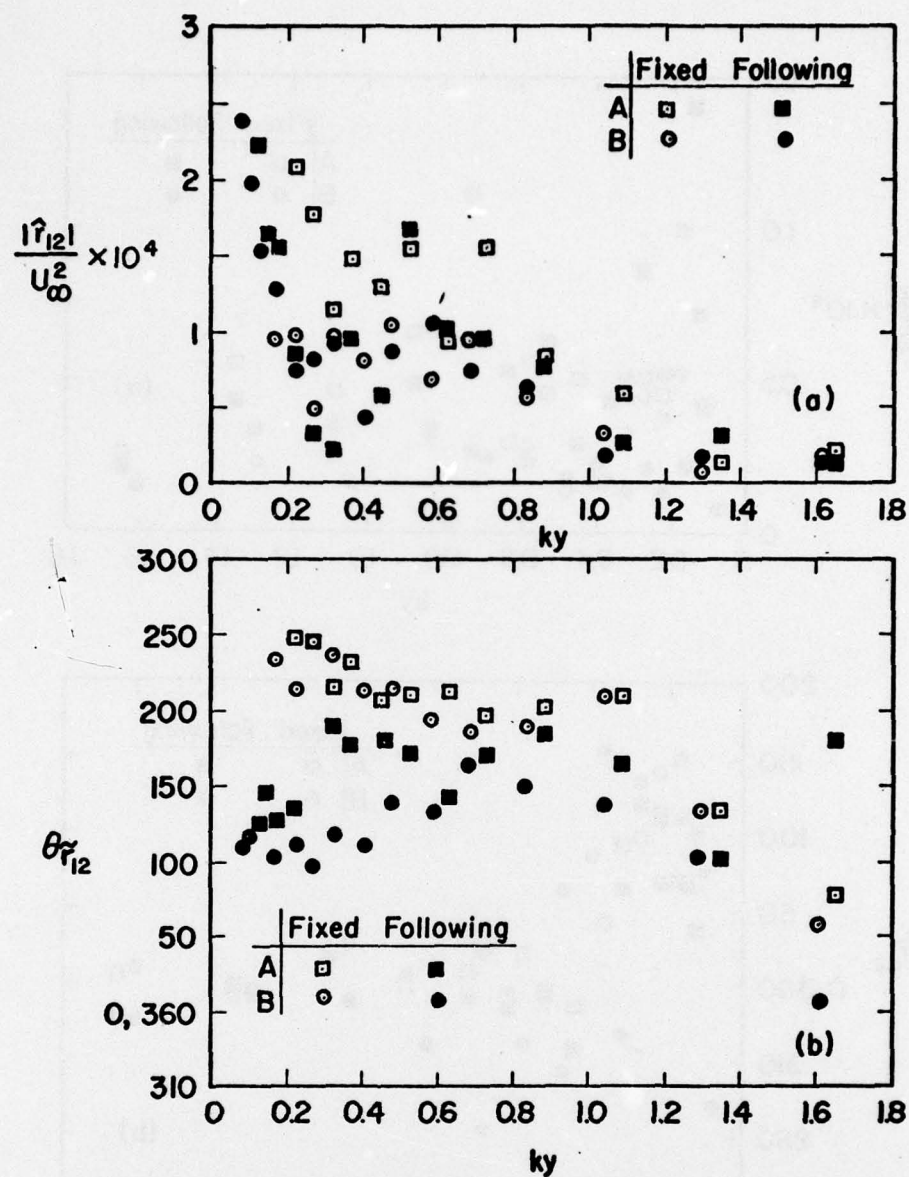


Figure 13. Amplitude and Phase Distributions for \tilde{r}_{12} at $U_{\infty}/c = 0.93$.

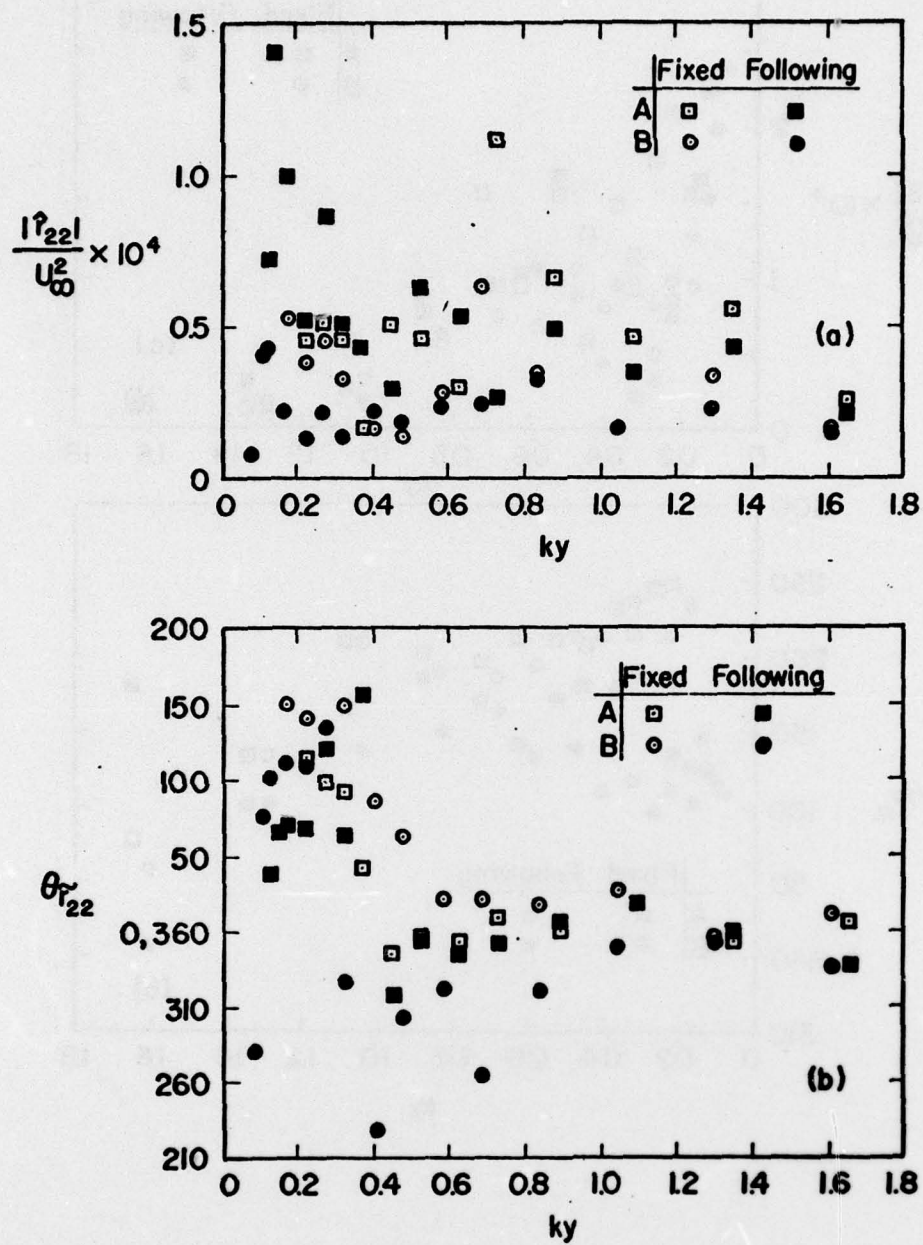


Figure 14. Amplitude and Phase Distributions for \tilde{r}_{22} at $U_\infty/c = 0.93$.

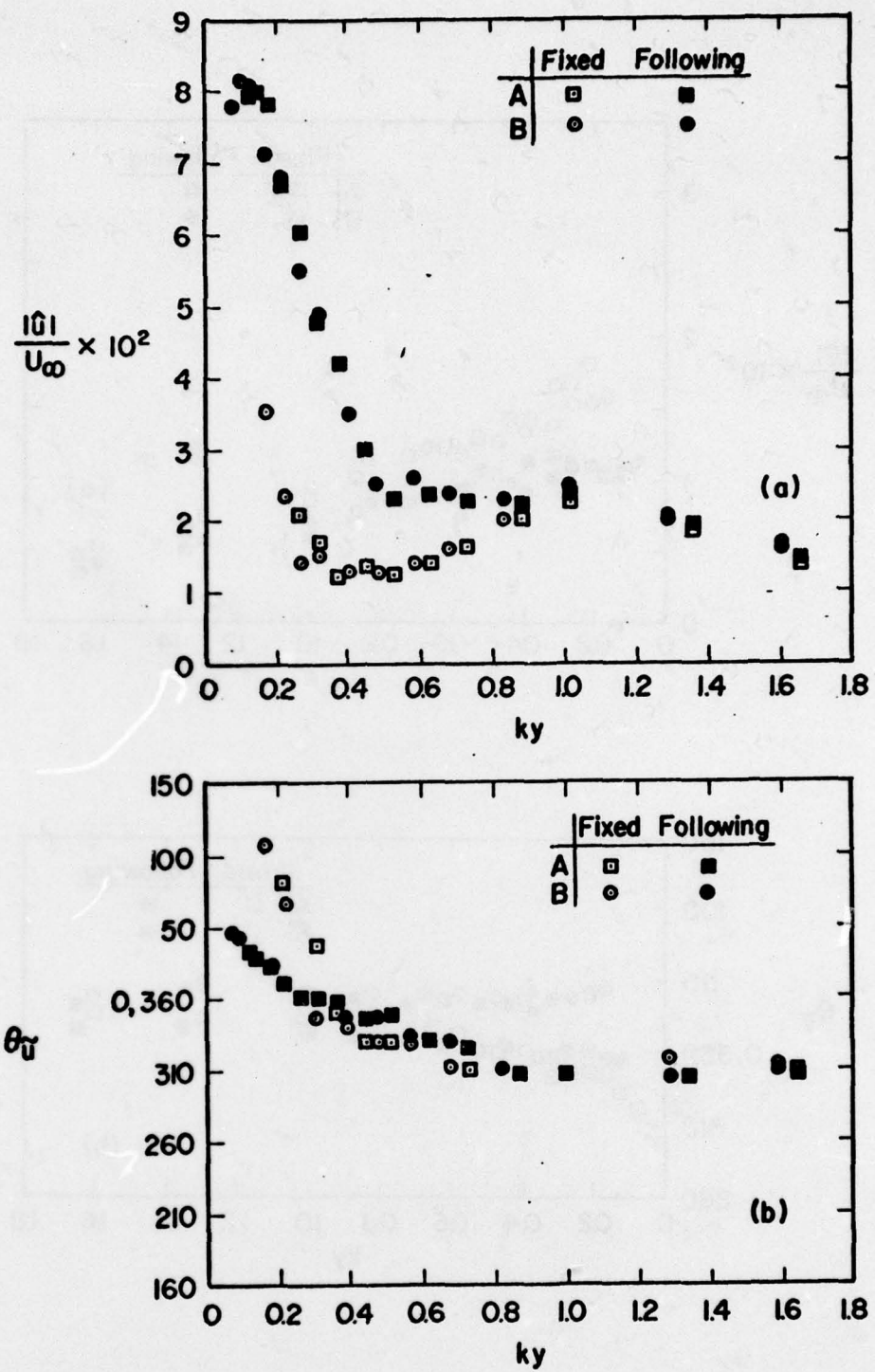


Figure 15. Amplitude and Phase Distributions for \tilde{u} at $U_\infty/c = 1.87$.

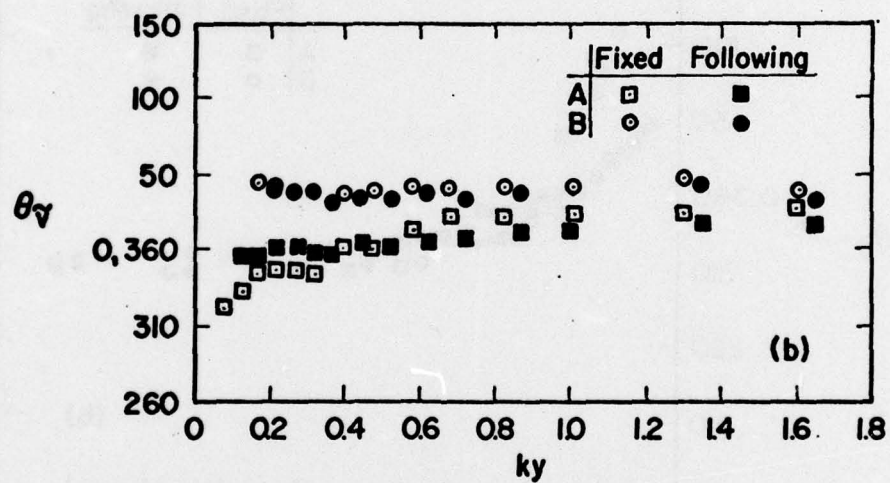
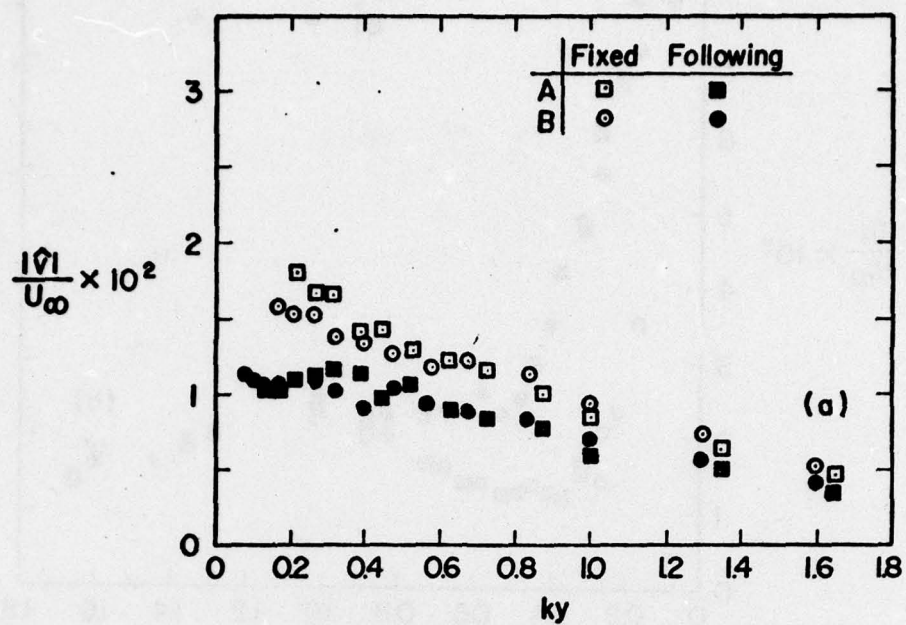


Figure 16. Amplitude and Phase Distributions for \tilde{v} at $U_\infty/c = 1.87$.

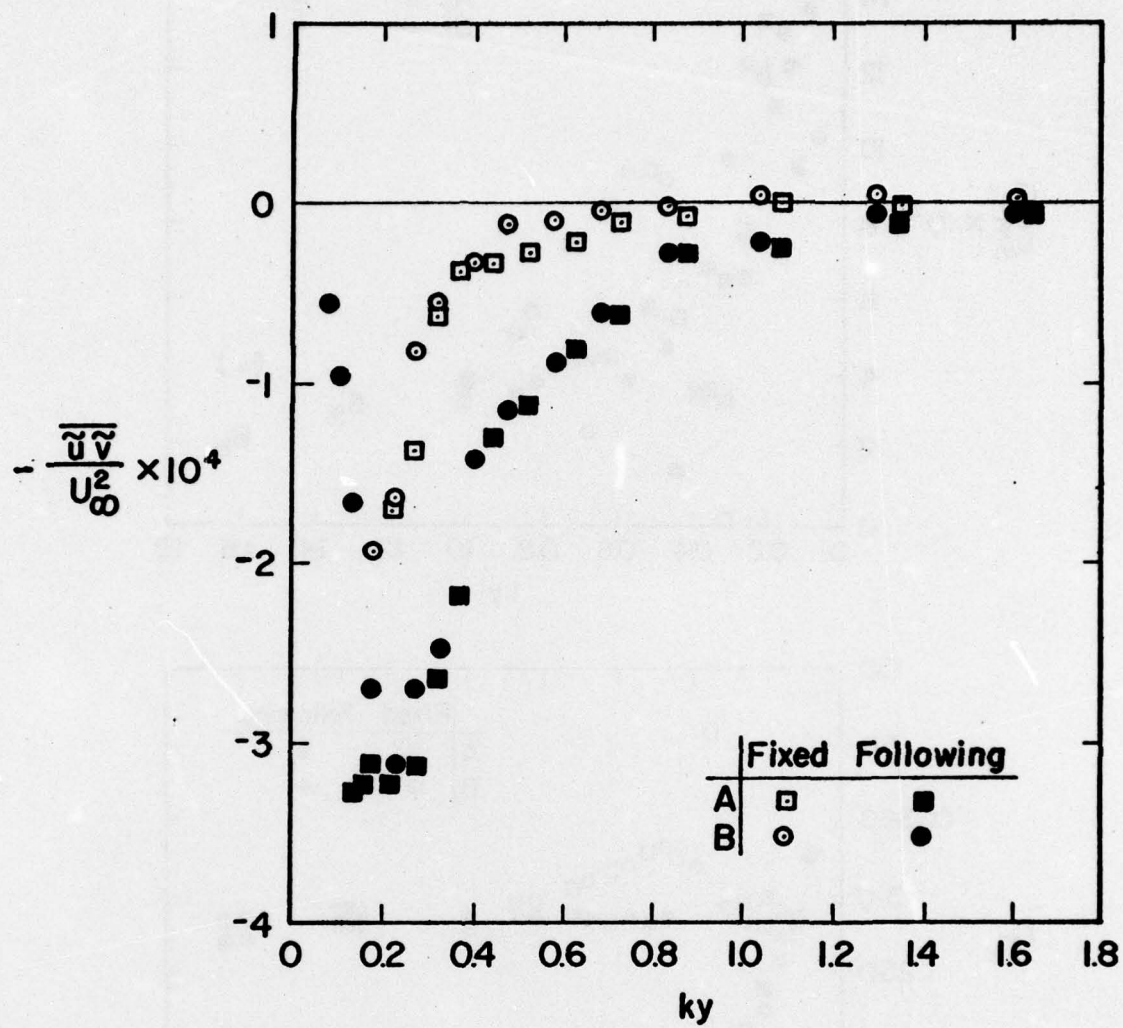


Figure 17. Distribution of the Wave-Associated Reynolds Stresses $-\overline{\tilde{u}\tilde{v}}$.
 $(U_\infty/c = 1.87)$

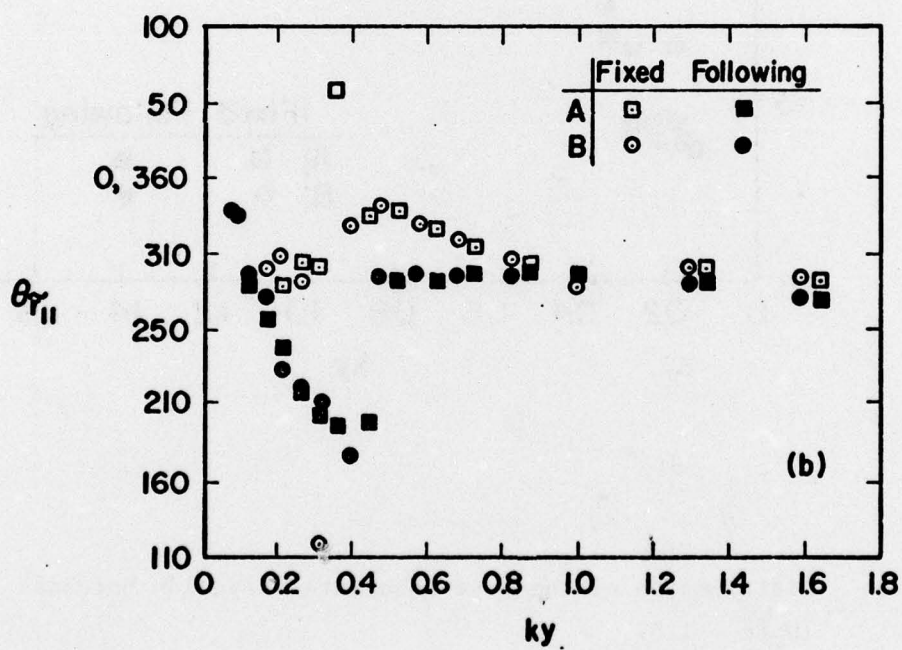
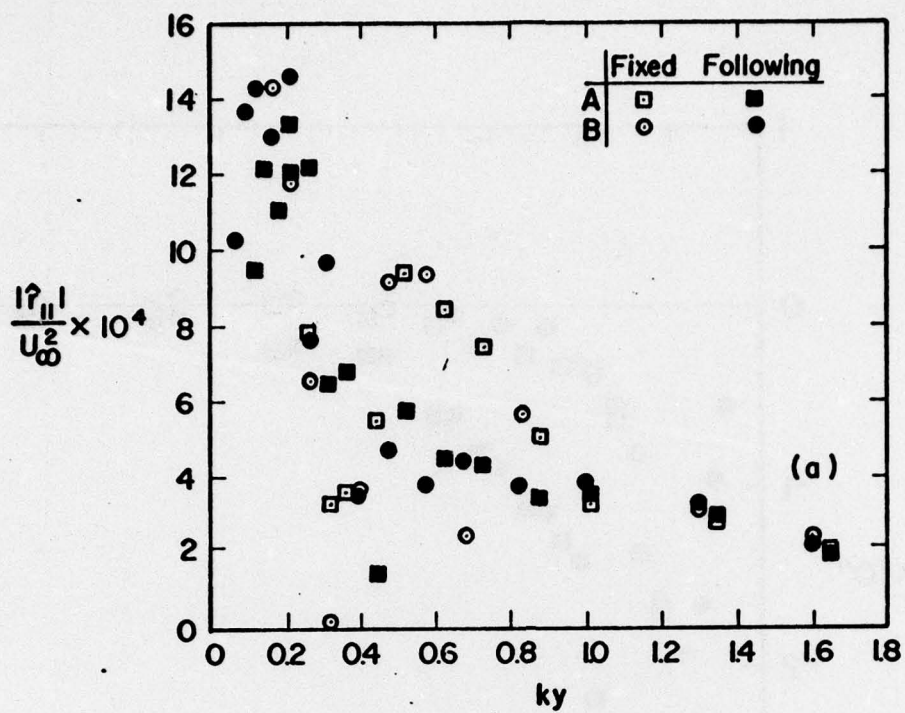


Figure 18. Amplitude and Phase Distributions for \tilde{r}_{11} at $U_{\infty}/c = 1.87$.

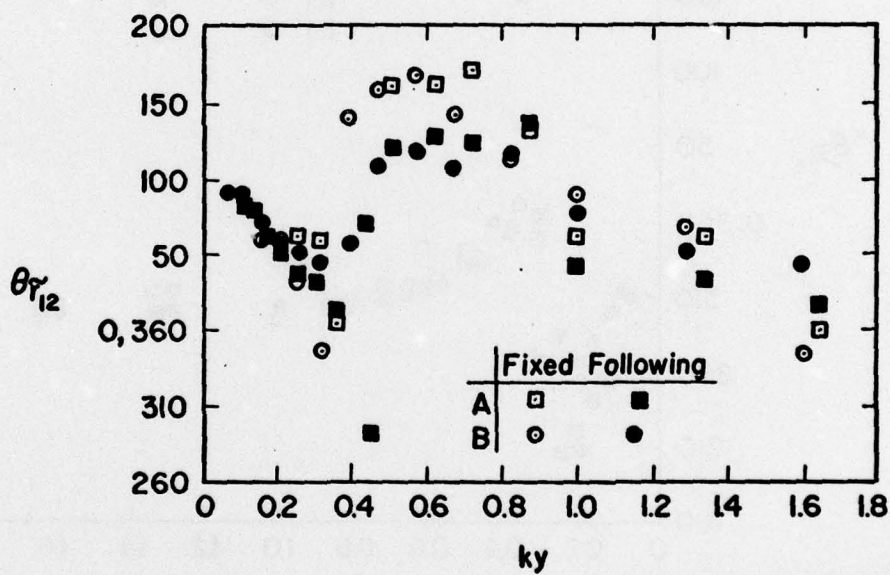
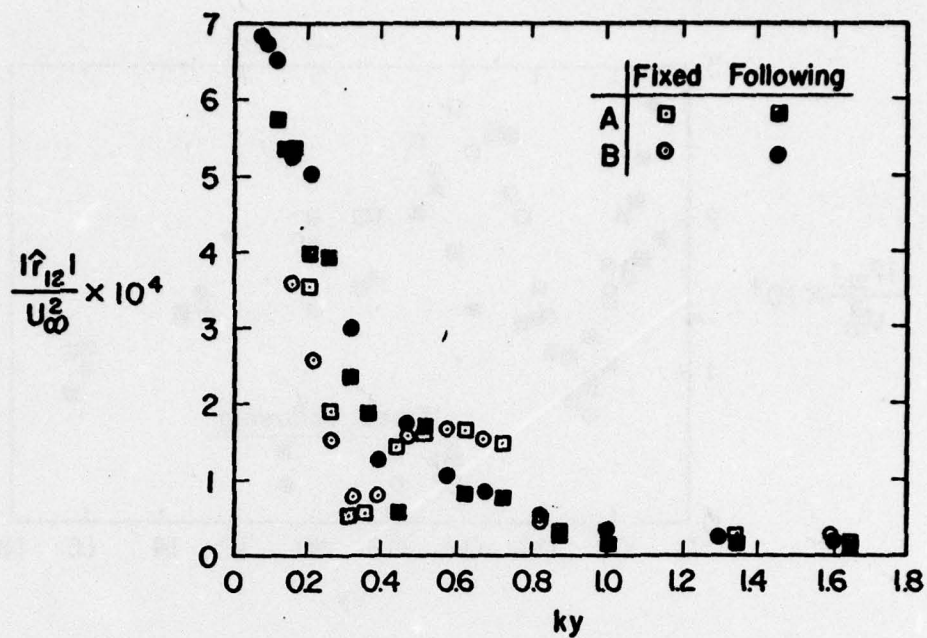


Figure 19. Amplitude and Phase Distributions for \tilde{r}_{12} at $U_\infty/c = 1.87$.

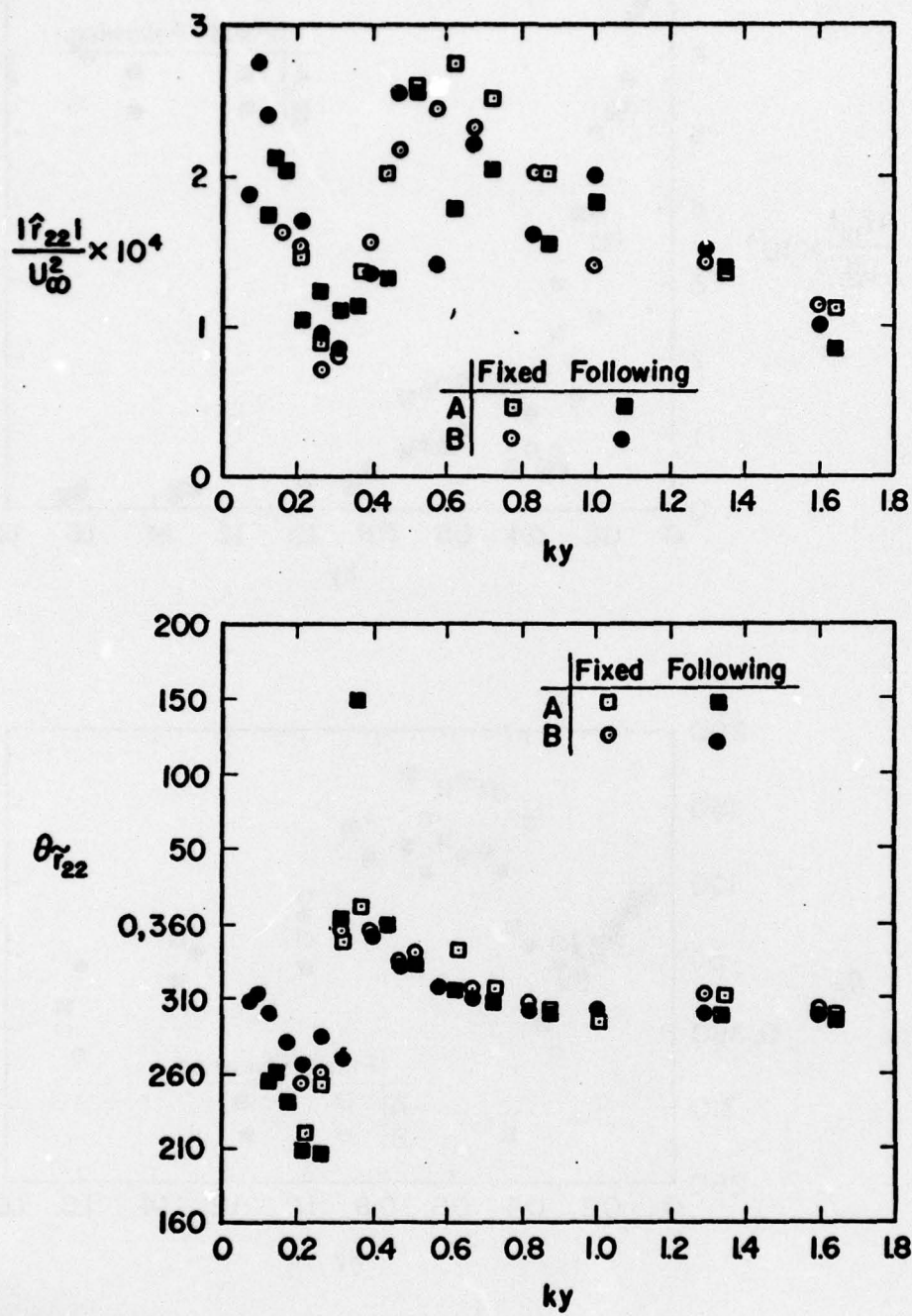


Figure 20. Amplitude and Phase Distributions for \tilde{r}_{22} at $U_{\infty}/c = 1.87$.